

Time Evolution of ML-MCTDH Wavefunctions II: Application of the Projector Splitting Integrator

Lachlan P Lindoy,^{1, a)} Benedikt Kloss,¹ and David R Reichman¹

Department of Chemistry, Columbia University, 3000 Broadway, New York, New York 10027, USA

The multi-layer multiconfiguration time-dependent Hartree (ML-MCTDH) approach suffers from numerical instabilities whenever the wavefunction is weakly entangled. These instabilities arise from singularities in the equations of motion (EOMs) and necessitate the use of a regularization parameter. The Projector Splitting Integrator (PSI) has previously been presented as an approach for evolving ML-MCTDH wavefunctions that is free of singularities. Here we will discuss the implementation of the multi-layer PSI with a particular focus on how the steps required relate to those required to implement standard ML-MCTDH. We demonstrate the efficiency and stability of the PSI for large ML-MCTDH wavefunctions containing up to hundreds of thousands of nodes by considering a series of spin-boson models with up to 10^6 bath modes, and find that for these problems the PSI requires roughly 3-4 orders of magnitude fewer Hamiltonian evaluations and 2-3 orders of magnitude fewer Hamiltonian applications than standard ML-MCTDH, and 2-3/1-2 orders of magnitude fewer evaluations/applications than approaches that use improved regularization schemes. Finally, we consider a series of significantly more challenging multi-spin-boson models that require much larger numbers of single-particle functions with wavefunctions containing up to $\sim 1.3 \times 10^9$ parameters to obtain accurate dynamics.

I. INTRODUCTION

In recent years considerable effort has been dedicated to addressing the ill-conditioning of the equations of motion (EOMs) of the single and multi-layer multi-configuration time-dependent Hartree methods.¹⁻⁴ The standard approach, in which the mean-field density matrix is regularized, works well in many situations, has been successfully applied to obtain the dynamics of a wide range of problems,⁵⁻²⁴ and a number of general purpose software packages have been developed that are capable of performing such calculations.^{25,26} However, as the types of problems considered grow larger in size and complexity, it has been found that there are regimes in which this strategy is not sufficient. These regimes include those with very large numbers of modes,²⁷ and those in which the Hamiltonian directly couples all modes together in a multiplicative fashion, as is the case in Fermionic MCTDH simulations²⁸ and in simulations of the polaron-transformed spin-boson model.^{2,3,29} For these situations, the regularized ML-MCTDH dynamics can depend strongly on components of the ML-MCTDH wavefunction that do not initially contribute to the expanded wavefunction,³⁰ can show “pseudoconvergence” (with respect to the regularization parameter) to incorrect dynamics,⁴ and can become extremely difficult to evolve numerically which in some extreme cases results in failure of the integrator.^{2,3} Recently, Wang and Meyer have presented an alternative strategy for regularizing the EOMs.^{3,27} Rather than regularize the mean-field density matrices, this approach regularizes the coefficient tensors. This approach has been applied to a wide range of spin-boson models and has been found to perform significantly better than the standard strategy. It

has been shown to be capable of treating very large systems and the polaron-transformed spin-boson model.^{3,27} While this approach has shown significant stability improvements over the standard regularization scheme, it still requires the solution EOMs that can be poorly conditioned depending on the value of the regularization parameter required. It is possible that there are regimes in which convergence with respect to the regularization parameter cannot be obtained before numerical issues arise in the solution of the EOMs.³¹

An alternative strategy for propagating ML-MCTDH wavefunctions is the projector splitting integrator (PSI) approach,³²⁻³⁴ originally presented by Lubich for single-layer MCTDH.^{35,36} This approach employs an alternative representation of the wavefunction when evolving the coefficient tensors, rendering the equations of motion singularity-free. Once this evolution has been performed, it is necessary to reconstruct the original representation, and in cases where the ML-MCTDH EOMs are singular this reconstruction is not fully specified. This is a fundamental issue for all ML-MCTDH approaches that are based on the linear variational principle and can only truly be resolved by going beyond linear variations.¹ However, in contrast to the standard ML-MCTDH EOMs, where this results in significant numerical instabilities, this process of reconstructing the original representation can be made numerically stable, albeit still partially arbitrary. It has been suggested that this arbitrariness may lead to problems with this approach. However, in principle, this approach could naturally be paired with the optimal unoccupied SPFs approach of Manthe¹ which defines an optimal reconstruction of the original representation. In practice, as we will demonstrate in this work, the arbitrary nature of the PSI does not significantly influence numerical performance, and issues arising from it can be considered to be convergence issues.

^{a)}Electronic mail: ll3427@columbia.edu

In what follows we will discuss the implementation of the multi-layer PSI, with a focus on how the steps required relate to those required to implement standard ML-MCTDH. Following this we will demonstrate the numerical performance of this approach by considering a range of challenging model problems in Sec. III. These problems include those that have previously been treated using an improved regularization scheme^{3,27} and represent ones for which standard ML-MCTDH can run into serious numerical issues, including the polaron-transformed spin-boson model and the standard spin-boson model with a large number of bath modes. Finally, we consider an application of the PSI to a series of multi-spin-boson models. These models require considerably larger coefficient tensors at each node of the ML-MCTDH wavefunction than is commonly treated using standard ML-MCTDH and represent considerably harder challenges than any previously treated spin-boson model. In addition to these, further results are presented in the Supplementary Information with the aim of addressing additional aspects of the convergence of the PSI.

II. THEORY

Before we discuss the implementation of the PSI, we will first briefly review the ML-MCTDH wavefunction and EOMs. In particular, we will discuss the recursive expressions for evaluating the terms present in the EOMs. By doing so we can directly relate the evaluation of analogous quantities required by the PSI to the standard ML-MCTDH quantities.

A. The ML-MCTDH Wavefunction Expansion and Trees

Instead of representing the wavefunction in the direct product basis of all the bases of the problem's degrees of freedom which requires an exponentially large number of wavefunction coefficients, ML-MCTDH expands the wavefunction in a hierarchy of time-dependent bases. The expansion coefficients of the latter are stored in a set of arrays, or tensors, which contain auxiliary indices in addition to the indices of the physical degrees of freedom. All tensors are connected to at least one other tensor through a shared index, i.e. the value of the index on both tensors is constrained to be the same in the expansion of the wavefunction (see Fig. 1). This defines a general loop-free network, and is referred to as a tree tensor network as its connectivity is described by a tree. Any node $z_l = (k_1 = 1, k_2, \dots, k_l)$, with l denoting the distance from the root node and k_j denoting the index of child node at the j -th layer of the tree, stands for a wavefunction coefficient tensor $A_{i_1 \dots i_{d^{z_l}} i_0}^{z_l}$, and we can interpret these objects as expansion coefficients in the basis defined by the remainder of the tree. Here i_0 represents the index of the array which connects this node to its parent node in the tree structure, that is it points towards

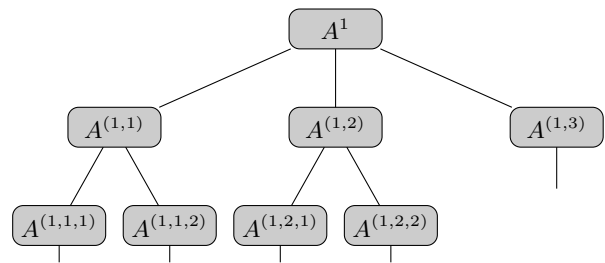


Figure 1. Representation of a tree tensor network for a five-dimensional wavefunction. Each node of the tree corresponds to a coefficient tensor, and the lines connecting nodes represent the contraction over indices common to the two nodes.

the root node, while the remaining d^{z_l} indices $i_1, \dots, i_{d^{z_l}}$ point towards the leaf nodes, i.e. the nodes at the bottom of the tree that are connected to the physical degrees of freedom. A subtree can be understood as containing a set of (time-dependent) basis functions, referred to as “single-particle functions” (SPFs), defined on the physical degrees of freedom that are in the subtree. In the ML-MCTDH context, it is usually understood that the physical degrees of freedom are located on the leaf nodes, however this restriction is not necessary. In analogy to a subtree encoding SPFs, we can think of the complement of the subtree as encoding basis functions for the physical degrees of freedom that are not in the subtree, the so called “single-hole functions” (SHFs).

The expression of a wavefunction in a ML-MCTDH format is non-unique since the product of a matrix M and its inverse M^{-1} can be inserted between any two coefficient tensor sharing a common index without changing the value of the wavefunction. However, we can impose gauge conditions on the tensors to remove this ambiguity. For example, we can, as is done in ML-MCTDH, require all non-root coefficient tensors satisfy the following orthonormality condition

$$A_{I^{z_l} i_0}^{*z_l} A_{I^{z_l} j_0}^{z_l} = \delta_{i_0 j_0} \quad \forall z_l \neq 1, \quad (1)$$

where we have introduced the notation $I^{z_l} = (i_1, \dots, i_{d^{z_l}})$ for the combined set of indices pointing towards the leaf nodes. We also note the use of Einstein summation convention, implying summation over repeated indices, in Eq. 1 and hereafter. This orthonormality condition translates to $A^{z_l} \forall z_l \neq 1$ being expansion coefficients for orthonormal SPFs in the direct product basis of orthonormal SPFs (or primitive basis functions for the leaf nodes) of the child nodes of z_l . The associated SHFs are not orthonormal, i.e. they have a non-unit overlap matrix, referred to as the mean-field density matrix. The mean-field density matrix at node z_l can be defined in terms of contractions between the SHFs of node z_l with their complex conjugate. This leads to a recursive definition of the $\rho^{(z_l, k)}$, the mean-field density matrix of the k -th child of node z_l (node (z_l, k)), in terms of the mean-field

density matrix ρ^{z_l} and coefficient tensor A^{z_l} of node z_l

$$\rho_{ab}^{(z_l, k)} = A_{I_{k;a}^{z_l}}^{*z_l} \rho_{i_j}^{z_l} A_{I_{k;b,j}^{z_l}}^{z_l}, \quad (2)$$

where $I_{k;a}^{z_l} = (i_1, \dots, i_{k-1}, a, i_{k+1}, \dots, i_{d^{z_l}})$ is a combined index obtained when the k th index in I^{z_l} is replaced with the value a . This expression makes use of Eq. 1 for all nodes that are not on the path between the root node and z_l . For the root node $z_l = 1$, Eq. 1 translates to A^1 being expansion coefficients for the full wavefunction in the orthonormal basis defined by the remainder of the tree, and it is not subject to any constraint besides normalization. To denote this special property, we will decorate its coefficient tensor with a *tilde*-symbol, namely \widetilde{A}^1 .

Having obtained an unambiguous ML-MCTDH representation of the wavefunction through the constraint in Eq. 1, we can treat the coefficient tensors as variational parameters and obtain a solution to the time-dependent Schrödinger equation using the time-dependent variational principle. To do this we need to further specify a dynamic gauge condition for the overlap of coefficient tensors with their time-derivative. Here, for simplicity, we will make use of the standard choice, namely that these two matrices are orthogonal for all nodes except the root node. This leads to the following EOMs for the coefficient tensor at the root node

$$\dot{\widetilde{A}}_{I^1}^1 = -\frac{i}{\hbar} \sum_r h_{r;I^1 J^1}^1 \widetilde{A}_{I^1}^1, \quad (3)$$

and at all other nodes

$$\dot{A}_{I^{z_l} i_0}^{z_l} = -\frac{i}{\hbar} \sum_r Q_{I^{z_l} K^{z_l}}^{z_l} h_{r;K^{z_l} J^{z_l}}^{z_l} A_{J^{z_l} j}^{z_l} H_{r;jk}^{z_l} [(\rho^{z_l})^{-1}]_{k i_0}. \quad (4)$$

Here, we have written the Hamiltonian in a sum-of-product (SOP) form, $\hat{H} = \sum_r \otimes_{a \in L} \hat{h}_r^a$, with L denoting the set of leaf nodes and \hat{h}_r^a is the Hamiltonian operator acting on the physical degree of freedom associated with leaf-node a . The Hamiltonian at each node can be expressed in terms of the matrices

$$\begin{aligned} h_{r;I^{z_l} J^{z_l}}^{z_l} &= \prod_{k=1}^{d^{z_l}} A_{I^{(z_l, k)} i_k}^{*(z_l, k)} h_{r;I^{(z_l, k)} J^{(z_l, k)}}^{(z_l, k)} A_{J^{(z_l, k)} j_k}^{(z_l, k)} \\ &= \prod_{k=1}^{d^{z_l}} M_{r; i_k j_k}^{(z_l, k)}, \end{aligned} \quad (5)$$

where $I^{(z_l, k)} = (i_1, \dots, i_d^{(z_l, k)})$ is the combined index for all indices associated with all children of node (z_l, k) , and

$$H_{r;ab}^{(z_l, k)} = A_{I_{k;a}^{z_l}}^{*z_l} \left(\prod_{\substack{k'=1 \\ k' \neq k}}^{d^{z_l}} M_{r; i_{k'} j_{k'}}^{(z_l, k')} \right) H_{r;ij}^{z_l} A_{I_{k;b,j}^{z_l}}^{z_l}. \quad (6)$$

The Hamiltonians in Eqs. 5 and 6 are referred to as the SPF and mean-field Hamiltonian matrices, respectively.

They can be considered as matrix elements of operators present in the SOP expansion evaluated using the SPFs and SHFs, respectively. Additionally, the projector onto the space spanned by the SPFs of node z_l appears in Eq. 4, and is defined as

$$Q_{I^{z_l} J^{z_l}}^{z_l} = \delta_{I^{z_l} J^{z_l}} - A_{I^{z_l} i}^{z_l} A_{J^{z_l} i}^{*z_l}. \quad (7)$$

The presence of this projector makes Eq. 4 non-linear. Furthermore, Eq. 4 contains the inverse of the mean-field density matrix, $(\rho^{z_l})^{-1}$. Since the density matrix is not guaranteed to be of full rank and is often almost rank-deficient, Eq. 4 can be singular and requires regularization of the matrix inverse in order to be numerically solvable.

B. Singularity-Free Versions of ML-MCTDH

In order to circumvent the presence of an ill-defined inverse in the ML-MCTDH EOMs, we can make use of the gauge freedom in the ML-MCTDH representation of the wave function. In particular, we can choose a representation in which both SHFs and SPFs for a given node z_l are orthonormal by imposing the following orthonormality condition

$$A_{I_{p(z_l);a}^{z_l}}^{*z_l} A_{I_{p(z_l);b}^{z_l}}^{z_l} = \delta_{ab} \quad \forall z_l \neq z_l, \quad (8)$$

where $p(z_l)$ indicates the index of the array which points towards node z_l , and $I_{p(z_l);a}^{z_l}$ is a combined index of the form used previously. For all nodes that are not node z_l or ancestors of node z_l (namely they are not its parent or parent's parent, and so on up to the root node), the index pointing to the p^{z_l} node is the same as the index pointing towards the root node ($p(z_l) = p(1)$). For these nodes Eq. 8 is equivalent to Eq. 1. For the nodes that are ancestors of node z_l , this corresponds to a different orthonormality condition. Imposing this condition alters the value of the coefficient tensors for these nodes. To make this explicit, we will choose a different label, U^{z_l} , for the coefficient tensors of nodes that satisfy Eq. 8 and are ancestors of node z_l . This orthogonality condition leads to orthonormal SPFs for all nodes which are not ancestors of node z_l , and orthonormal SHFs for node z_l and all of its ancestors. The latter property can be straightforwardly verified by comparison with Eq. 2. Note that Eq. 1 is obtained as a special case ($z_l = 1$) of Eq. 8.

Singularity-free approaches to propagating the ML-MCTDH wavefunction make use of this representation, in which the inverse of the density matrix ρ^{z_l} is trivially the identity matrix. In the following, we will discuss a particular singularity-free method to propagate ML-MCTDH wavefunctions, the projector splitting integrator (PSI). This algorithm can be considered as a linearized integrator for singularity-free ML-MCTDH EOMs, similar to the commonly used constant-mean-field integrator for standard ML-MCTDH EOMs. Instead of solving Eq. 4

for the non-root node coefficient tensors under the orthonormality constraint Eq. 1, the PSI involves solving two differential equations for every node z_l serially, that is node-by-node. First, we propagate the coefficient tensor \tilde{A}^{z_l} forward in time, where the *tilde*-symbol indicates that we enforce orthonormality condition in Eq. 8 for node z_l according to

$$\dot{\tilde{A}}_{I^{z_l}i_0}^{z_l}(t) = -\frac{i}{\hbar} \sum_r h_{r;I^{z_l}J^{z_l}}^{z_l} \tilde{A}_{J^{z_l}j}^{z_l}(t) \tilde{H}_{rj i_0}^{z_l}. \quad (9)$$

Here, we explicitly denote time-dependence, and the other quantities are taken to be time-independent, which renders Eq. 12 linear. *Tilde*-symbols on the SHF Hamiltonian matrices are used to indicate that these quantities are evaluated using orthonormal SHFs. The SPF Hamiltonian matrix elements are unchanged from those in Eq. 4. Note that the structure of Eq. 9 is similar to Eq. 4, with the exception of the omission of the mean-field density matrix inverse, which is trivially the identity matrix due to the chosen orthonormality condition and the second term in projector Q^{z_l} (see Eq. 7). Second, we use an orthogonal decomposition

$$\tilde{A}_{I^{z_l}i_0}^{z_l} = A_{I^{z_l}j_0}^{z_l} R_{j_0i_0}^{z_l} \quad | \quad A_{I^{z_l}j_0}^{*z_l} A_{I^{z_l}j'_0}^{z_l} = \delta_{j_0,j'_0}, \quad (10)$$

which gives a different orthonormality condition,

$$\begin{aligned} U_{I_{p(z_l)a}^{z_l}i}^{*z_l} U_{I_{p(z_l)b}^{z_l}i}^{z_l} &= \delta_{ab} \quad \forall z_l \in \text{ancestors}(z_l), \\ A_{I^{z_l}i}^{*z_l} A_{I^{z_l}j}^{z_l} &= \delta_{ij} \quad \forall z_l \notin \text{ancestors}(z_l), \end{aligned} \quad (11)$$

where $\text{ancestors}(z_l)$ denotes the set of nodes that are ancestors of node z_l . We can interpret R^{z_l} as an additional, temporary node in the tree. We propagate R^{z_l} backwards in time according to

$$\dot{R}_{ij}^{z_l}(t) = -\frac{i}{\hbar} \sum_r A_{K^{z_l}i}^{*z_l} h_{r;K^{z_l}J^{z_l}}^{z_l} A_{J^{z_l}k}^{z_l} R_{kl}^{z_l}(t) \tilde{H}_{r;l j}^{z_l}. \quad (12)$$

The structure of Eq. 12 is again similar to that of Eq. 4, with the exception that Eq. 12 only accounts for the non-trivial term in projector Q^{z_l} and the lack of the inverse of the density matrix due to the chosen orthonormality condition. The fact that this equation is solved backwards in time stems from the negative sign in front of the second term in projector Q^{z_l} . The requirement to solve Eqs. 9 and 12 sequentially, one node at a time, arises from the change of orthonormality conditions associated with propagating different nodes. Note that seriality is not inherently necessary for singularity-free approaches, as discussed in the companion paper and in Refs. 4 and 37.

The PSI involves the changing of orthonormality conditions between different nodes interspersed with the solution of linear differential equations. In the following, we will introduce how to efficiently convert between ML-MCTDH wavefunctions with different orthonormality conditions before discussing the algorithm in detail.

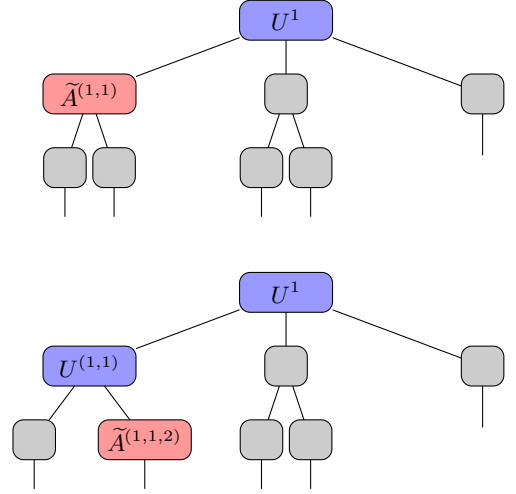


Figure 2. Diagrammatic representations of the ML-MCTDH wavefunction from Fig. 1 transformed into the alternative representation where both the SPF and SHFs of node z_l are orthonormal. For the top tree $z_l = (1, 1)$, while for the bottom tree $z_l = (1, 1, 2)$. The coefficient tensors of the unlabelled (grey) nodes satisfy the orthonormality condition given in Eq. 1, and are left unchanged by this transformation. The coefficient tensors of the nodes labelled with U^{z_l} (blue) satisfy the orthonormality condition given in Eq. 8, and so will generally differ from the standard coefficient tensors. Finally, the coefficient tensors labelled with \tilde{A}^{z_l} (red) are the transformed coefficient tensors given by Eq. 10 that evolves according to the EOM given in Eq. 9.

C. Conversion Between Different Orthonormality Conditions and Update of Hamiltonian Matrix Elements

The orthonormality condition used in ML-MCTDH (Eq. 1) is just the special case of the orthonormality condition given in Eq. 8 when $z_l = 1$. In order to be able to convert between Eq. 1 and Eq. 8 for any arbitrary z_l and back, there are two operations we need to perform:

- Given that Eq. 8 holds for node z_l we need to be able to convert to a representation where it holds for the child node (z_l, k) for any value of k .
- Given that Eq. 8 holds for the node (z_l, k) we need to be able to convert to a representation where it holds for its parent node z_l .

We will begin by assuming that we have a representation in which Eq. 8 holds for node z_l , and present how to transform the ML-MCTDH wavefunction so that this condition is enforced for a child node (z_l, k) . In order to do this we need to construct a new coefficient tensor U^{z_l} for node z_l so that the orthogonality condition in Eq. 8 is satisfied for node (z_l, k) . This tensor is related to the coefficient tensors \tilde{A}^{z_l} by multiplication with a matrix $R^{(z_l, k)}$,

$$\tilde{A}_{I_{k;b}^{z_l}i}^{z_l} = U_{I_{k;a}^{z_l}i}^{z_l} R_{ba}^{(z_l, k)} \quad | \quad U_{I_{k;a}^{z_l}i}^{*z_l} U_{I_{k;b}^{z_l}i}^{z_l} = \delta_{ab}. \quad (13)$$

Note that the decomposition given in Eq. 13 is not unique, which can be seen by inserting $I = U^{-1}U$ with a unitary U between $R^{(z_l, k)}$ and \tilde{U}^{z_l} . There are arbitrarily many matrices that provide equally valid decompositions. For instance, one could apply a QR matrix decomposition on \tilde{A}^{z_l} , reshaped as a matrix of size

$$\left(\prod_{\substack{j=0 \\ j \neq k}}^{d^{z_l}} n_j^{z_l} \right) \times n_k^{z_l}, \quad (14)$$

with $n_0^{z_l} = N^{z_l}$, which returns a unique decomposition with $R^{(z_l, k)}$ an upper triangular matrix if \tilde{A}^{z_l} does not have linearly dependent columns. If \tilde{A}^{z_l} does have linearly dependent columns, the corresponding entries in U^{z_l} can be chosen freely as long as they constitute orthonormal columns. Contracting the matrix $R^{(z_l, k)}$ with the coefficient tensor at node (z_l, k) ,

$$A_{I^{(z_l, k)}_{j_0}}^{(z_l, k)} R_{j_0 i_0}^{(z_l, k)} = \tilde{A}_{I^{(z_l, k)}_{i_0}}^{(z_l, k)}, \quad (15)$$

leaves us with an expansion of the wavefunction in terms of orthonormal SPFs and SHFs for node (z_l, k) . Since we have modified the coefficient tensor of the node z_l , we need to update the mean-field Hamiltonian matrix elements for node (z_l, k) ,

$$\tilde{H}_{r;ab}^{(z_l, k)} = U_{I_{k;a}^{z_l} i}^{*z_l} \left(\prod_{\substack{k'=1 \\ k' \neq k}}^{d^{z_l}} M_{r;i_k' j_k'}^{(z_l, k')} \right) \tilde{H}_{r;ij}^{z_l} U_{I_{k;b}^{z_l} j}^{z_l}, \quad (16)$$

where $M_{r;i_k' j_k'}^{(z_l, k')}$ is defined in Eq. 5, and in order to ensure we can apply this equation for all nodes in the tree, we will define $\tilde{H}_{r;ij}^1 = 1$ for $i = j = 1$. Note that this equation is very closely related to the standard ML-MCTDH expression for the mean-field matrix $H_r^{(z_l, k)}$ for a child of node z_l , Eq. 6. It is the same expression but with A^{z_l} replaced with U^{z_l} . As such, the process for evaluating these matrices does not change significantly when compared to standard ML-MCTDH, other than that some additional optimizations become possible due to the orthonormality of these SHFs (see Sec. IV of the Supplementary Information). Note that when transferring the orthogonality condition to a child node, the SPF Hamiltonian matrices for the child node remain unchanged and do not need to be updated.

The reverse operation, converting the orthogonality condition from node (z_l, k) to its parent node z_l proceeds as follows. First, a decomposition of the form given in Eq. 10 is obtained,

$$\tilde{A}_{I^{(z_l, k)}_{i_0}}^{(z_l, k)} = A_{I^{(z_l, k)}_{j_0}}^{(z_l, k)} R_{j_0 i_0}^{(z_l, k)} \quad | \quad A_{I^{(z_l, k)}_{j_0}}^{(z_l, k)*} A_{I^{(z_l, k)}_{j'_0}}^{(z_l, k)} = \delta_{j_0 j'_0}. \quad (17)$$

Then the SPF Hamiltonian matrices for node z_l are up-

dated according to

$$h_{r;I^{z_l} J^{z_l}}^{z_l} = \prod_{k=1}^{d^{z_l}} A_{I^{(z_l, k)}_{i_k}}^{*(z_l, k)} h_{r;I^{(z_l, k)} J^{(z_l, k)}}^{(z_l, k)} A_{J^{(z_l, k)}_{j_k}}^{(z_l, k)}, \quad (18)$$

which is exactly the same expression as in the standard ML-MCTDH case. Finally we contract $R^{(z_l, k)}$ with U^{z_l} ,

$$\tilde{A}_{I_{k;b}^{z_l} i}^{z_l} = R_{ba}^{(z_l, k)} U_{I_{k;a}^{z_l} i}^{z_l}. \quad (19)$$

When transferring the orthogonality condition to the parent of node z_l , the SHF Hamiltonian matrices for the parent remain unchanged and do not need to be updated, while the SHF Hamiltonian matrices for node z_l do not appear in the algorithm's working equations and thus do not need to be recomputed.

In calculations it is not necessary to form the SPF Hamiltonian matrices $h_r^{z_l}$, all required operations can be expressed in terms of the matrices $M_r^{(z_l, k)}$ associated with the child nodes of node z_l . The SPF Hamiltonian matrix is the Kronecker product of each of these matrices. This representation leads to an efficient scheme for applying the SPF Hamiltonian matrix to the coefficient tensors in terms of a series of matrix-tensor contractions. Additionally, it is useful to make use of an alternative SOP form as discussed in Sec. IV of the Supplementary Information.

We can convert a ML-MCTDH wavefunction for which Eq. 8 is satisfied for node z_l to one for which it is satisfied for node z'_l by performing the above operations sequentially along the path through the tree that connects nodes z_l and z'_l .

D. Integrating the Singularity-Free Equations of Motion: the Projector Splitting Integrator

The PSI propagates the coefficient tensor at node z_l , A^{z_l} , for a fixed time step dt using a wavefunction expansion with orthonormal SPFs and SHFs for node z_l , while keeping the coefficient tensors at other nodes constant during the update at node z_l . Neglecting the time dependence of quantities involving other coefficient tensors is similar in spirit to the well-established constant mean-field (CMF) integration scheme for the standard ML-MCTDH EOMs, with the exception that the PSI updates the coefficients at the nodes sequentially. The order in which nodes are propagated is in principle arbitrary. Here we will discuss an efficient and easily illustrated order, namely an Euler tour traversal,³⁸ starting from the root node. For the single-layer case this traversal reduces to the previously published version for MCTDH wavefunctions.³⁶ In analogy with the single-layer version, a symmetric, second-order integrator is obtained by combining a propagation step with its adjoint. Specifically, this means that a single time-step consists of two sub-steps: a forward and a backward walk through the tree structure, each of which propagates all coefficient tensors by $dt/2$. We restate the equations of motion to be solved

for the reader's convenience expressed using the matrix notation employed in the companion paper:

$$\dot{\tilde{\mathbf{A}}}^{z_l}(t) = -\frac{i}{\hbar} \sum_r \mathbf{h}_r^{z_l} \tilde{\mathbf{A}}^{z_l}(t) \widetilde{\mathbf{H}}_r^{z_l}, \quad (20)$$

and

$$\dot{\mathbf{R}}^{z_l}(t) = -\frac{i}{\hbar} \sum_r \mathbf{A}^{z_l\dagger} \mathbf{h}_r^{z_l} \mathbf{A}^{z_l} \mathbf{R}^{z_l}(t) \widetilde{\mathbf{H}}_r^{z_l}, \quad (21)$$

for $z_l \neq 1$, and

$$\dot{\tilde{\mathbf{A}}}^1(t) = -\frac{i}{\hbar} \mathbf{h}^1 \tilde{\mathbf{A}}^1(t) \quad (22)$$

for the root node coefficient tensor. The integrator is described schematically in Fig. 3 and verbally in the following paragraphs.

Forward walk: The forward walk starts and ends with a wavefunction that fulfills Eq. 8 for the root node $z_l = 1$. The walk on the tree is counter-clockwise, namely the next node will always be the closest to the last visited node in a counter-clockwise direction. This ensures that every link on the tree is traversed exactly twice, once while descending and once while ascending. The first node visited after the root node is its leftmost child node. During the forward walk, descending the tree only involves transferring the orthonormality condition given by Eq. 8 from node z_l to the next node (one of its children), according to the procedure outlined above. Furthermore, we update the mean-field Hamiltonian matrix elements, $\widetilde{\mathbf{H}}_r^{z_l}$, to be consistent with the current expansion of the wavefunction (see Eq. 13). When the walk ascends from node (z_l, k) to node z_l , we solve the EOMs Eqs. 20 and 21. Specifically, we propagate $\tilde{\mathbf{A}}^{(z_l, k)}(t_0)$ to $\tilde{\mathbf{A}}^{(z_l, k)}(t_0 + dt/2)$ using Eq. 20 and for all non-root nodes use the decomposition $\tilde{\mathbf{A}}^{(z_l, k)}(t_0 + dt/2) = \mathbf{A}^{(z_l, k)}(t_0 + dt/2) \mathbf{R}^{(z_l, k)}(t_0 + dt/2)$ (see Eq. 17). After updating SPF Hamiltonian matrix elements of node z_l using $\mathbf{A}^{(z_l, k)}(t_0 + dt/2)$ (see Eq. 18), we propagate $\mathbf{R}^{(z_l, k)}(t_0 + dt/2)$ backwards in time to $\mathbf{R}^{(z_l, k)}(t_0)$ using Eq. 21. Contracting $\mathbf{R}^{(z_l, k)}(t_0)$ with the coefficient tensor of node z_l establishes the orthogonality condition Eq. 8 for node z_l and completes the step from node (z_l, k) to z_l .

Backward walk: The backward walk starts and ends with a wavefunction that fulfills Eq. 8 for $z_l = 1$, i.e. at the root node. The walk on the tree is clockwise, i.e. the next node is the closest to the last visited node in a clockwise direction. During the walk, every link on the tree is traversed exactly twice, once while descending and once while ascending. The first node visited after the root node is its rightmost child node. During the backward walk, ascending the tree only involves transferring the orthonormality condition given by Eq. 8 from a node (z_l, k) to its parent node z_l . Furthermore, we will update the SPF Hamiltonian matrix elements, $\mathbf{h}_r^{z_l}$, to be consistent with the current expansion

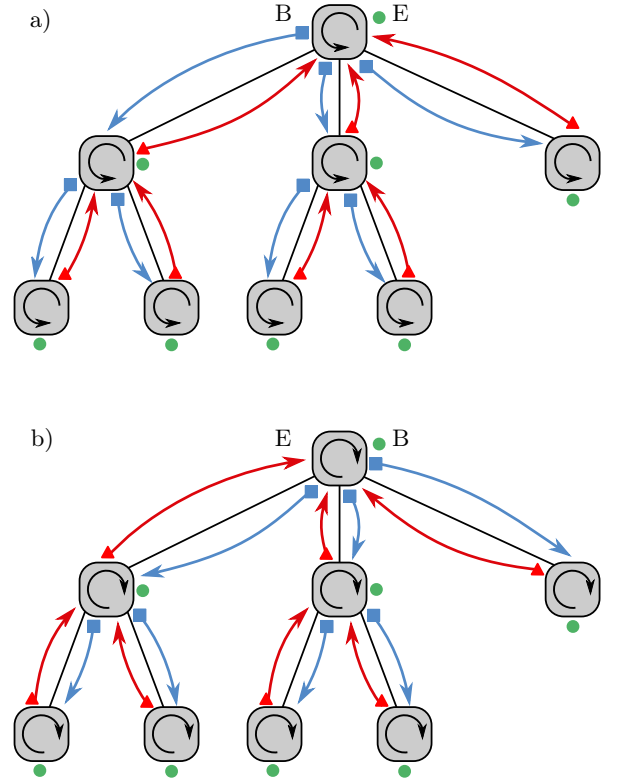


Figure 3. The two node traversal schemes used in the implementation of the PSI described in this work. a) Represents the forward walk step. b) Representation of the backwards walk step. The blue squares correspond to the construction of the orthonormal SHFs followed by the updating of mean-field matrices. The green circles correspond to evolution of the transformed coefficient tensors. The red triangles correspond to reformation of the standard coefficient tensors. The arrows connecting nodes correspond to transfers of the non-orthogonal $\mathbf{R}^z(t)$ matrix between nodes of the tree, and the black arrows in each node indicate the order in which these operations occur, e.g. operations on a node are applied counter-clockwise in the forward step and clockwise in the backwards step. For both walks the beginning (B) and end (E) points are shown.

of the wavefunction (see Eq. 18). When the walk descends from node z_l to node (z_l, k) , we solve the EOMs Eqs. 20 and 21. Specifically, we obtain $\mathbf{R}^{(z_l, k)}$ by decomposing $\tilde{\mathbf{A}}^{z_l}$ according to Eq. 13, update the mean-field matrix elements for node (z_l, k) (see Eq. 16) and propagate $\mathbf{R}^{(z_l, k)}$ backwards in time from $\mathbf{R}^{(z_l, k)}(t_0 + dt)$ to $\mathbf{R}^{(z_l, k)}(t_0 + dt/2)$ using Eq. 21. $\mathbf{R}^{(z_l, k)}(t_0 + dt/2)$ is contracted with $\mathbf{A}^{(z_l, k)}(t_0 + dt/2)$ (see Eq. 15), yielding $\tilde{\mathbf{A}}^{(z_l, k)}(t_0 + dt/2)$ and restoring the orthogonality condition Eq. 8 for node (z_l, k) . $\tilde{\mathbf{A}}^{(z_l, k)}(t_0 + dt/2)$ is propagated forward in time according to Eq. 20, which completes the step from node z_l to (z_l, k) .

E. Discussion of the PSI

The PSI can be readily implemented within existing ML-MCTDH implementations. Since the working equations are similar to those employed in standard ML-MCTDH, the only components which may not already be part of the code are the Euler tour traversal and the orthonormal decomposition of coefficient tensors in Eq. 13. Algorithms for the former are readily available,³⁸ and efficient linear algebra routines to perform an orthogonal matrix decomposition are part of most linear algebra packages. Employing the latter requires reshaping of the coefficient tensor into a matrix with size given by Eq. 14, with k chosen as required.

A potential drawback of the PSI presented here is its inherent seriality. CMF schemes for ML-MCTDH on the other hand allow for straightforward parallel integration. Parallel versions of the PSI should be possible to construct, with a version for single-layer MCTDH having already been proposed³⁷ and a related scheme having been discussed for ML-MCTDH.⁴ At present, such approaches tend to require much smaller time steps than the PSI (see Sec. II of the Supplementary Information), which largely negates the speedup obtained through parallelization in many cases.

The PSI has been shown to be stable with respect to almost or fully rank deficient wavefunction parametrizations in its MCTDH³⁶ and ML-MCTDH formulations,^{31,33,34,39} including the important subcategory of matrix product states (maximally layered trees with physical degrees of freedom at each layer).^{32,40,41} The stability of the PSI with respect to nearly rank-deficient wavefunction parametrizations can be attributed to the fact that the EOMs solved are always well-conditioned. In ML-MCTDH, the regularization parameter controls how ill-conditioned the equations are and how rapidly the variational parameters with vanishing weight in the wavefunction expansion evolve. In addition, it influences the weight above which the evolution of these parameters becomes accurate. The PSI on the other hand has no adjustable parameter except for time-step size, and rank-deficiency leads to non-uniqueness of the orthogonal decomposition but does not increase the stiffness of the underlying EOMs. In exceptional cases, any ML-MCTDH approach can suffer from inaccurate results for certain choices of initial unoccupied SPFs⁴² and the PSI could additionally show dependence on the choice of redundant parameters in the orthogonal decompositions. We will provide numerical evidence in the following that this effect can be suppressed by simply increasing the number of SPFs.

The following section will address the lack of benchmarks and demonstrate the stability and performance of the PSI in a set of typical applications of ML-MCTDH. Before we move on, we would like to point to developments towards a dynamical adaption of the number of SPFs at each node of the ML-MCTDH expansion during the propagation.^{29,43-45} These approaches

can speed up challenging calculations, but more importantly algorithms that make use of higher powers of the Hamiltonian^{29,44} address, at least partially, the fundamental shortcoming of the time-dependent variational principle. They provide information about the optimal evolution of redundant variational parameters, however at the cost of requiring the evaluation of the action of higher powers of the Hamiltonian on the wavefunction. While some of these approaches have been formulated for matrix product states, they are equally applicable to generic ML-MCTDH wavefunctions.

III. RESULTS

In order to demonstrate the capabilities of the PSI, we will consider a series of 3 models. The first, a simple two-dimensional bi-linearly and bi-quadratically coupled harmonic oscillator model, will be used to explore the extent to which the choice of unoccupied SPFs influences the dynamics obtained. The second set of models will be a series of spin-boson models with strong system-bath coupling and varying numbers of bath modes. This set of models will be used to demonstrate the effect that increasing the bath size has on the convergence properties of the PSI and how well the PSI can treat Hamiltonians with terms that couple all modes to all other modes. The final set of models that will be considered are a series of multi-spin-boson models with varying numbers of two-level systems (TLSs). These models will serve as a test of the PSI when larger number of SPFs are required at each node.

A. Two-Dimensional, Bi-Linearly and Bi-Quadratically Coupled Harmonic Oscillator Model

We start by considering a two-dimensional oscillator model that is described by the Hamiltonian¹

$$\hat{H} = \frac{1}{2} \left(-\frac{\partial^2}{\partial x^2} + x^2 \right) + \frac{1}{2} \left(-\frac{\partial^2}{\partial y^2} + y^2 \right) + \frac{1}{4}xy + \frac{1}{2} \left(x^2 - \frac{1}{2} \right) \left(y^2 - \frac{1}{2} \right). \quad (23)$$

This model is particularly useful when assessing the behavior of unoccupied SPFs. When the initial wavefunction is taken to be the non-interacting ground state, ($\Psi_0(x, y) = \chi_0(x)\chi_0(y)$, where χ_n is the n -th eigenfunction of the unitless one-dimensional harmonic oscillator), it is possible to evaluate the optimal unoccupied SPFs analytically, and their short time evolution, giving¹

$$\phi_{opt}^{(1)}(z) = \chi_2(z), \quad (24)$$

$$\phi_{opt}^{(2)}(z) = \chi_1(z), \quad z = x, y. \quad (25)$$

For short times, the first of these function will provide the dominant correction to the evolution of the wavefunction and will be referred to as the dominant unoccupied

SPF. In Ref. 1, it was demonstrated that when two SPFs are used for each mode, the dynamics obtained by conventional MCTDH are sensitive to the choice of the initially unoccupied SPF. The dynamics obtained using the PSI has also been shown to exhibit a dependence on the initially unoccupied SPFs.³⁶ When the unoccupied SPF initially has considerable overlap with the non-dominant unoccupied SPF, Eq. 25, it may not capture the dominant contribution to the dynamics. It should be noted that in these tests, only a very specific set of initial conditions are considered.

Here we consider a series of different initial configurations in an attempt to further explore the dependence on initial conditions. We will employ a N_{hilb} -dimensional Hilbert space of harmonic oscillator basis functions for each mode and uniformly sample normalized unoccupied SPFs within the space that is orthogonal to the harmonic oscillator ground state. In Table I, we present the percentage of wavepacket evolutions (out of a total of 1000) in which the unoccupied SPF did not evolve following the dominant unoccupied SPFs. When using two SPFs per

N_{SPF}	2			
N_{hilb}	10	10^2	10^3	10^4
$\%_f$	0	0	1.2	10.8

N_{SPF}	3			
N_{hilb}	10	10^2	10^3	10^4
$\%_f$	0	0	0	0

Table I. The percentage of wavepacket evolutions ($\%_f$) where the unoccupied SPFs failed to evolve following the dominant unoccupied SPF for different local Hilbert space dimensions (N_{hilb}). 1000 wavepacket evolutions were performed for each case with the initial states of the unoccupied SPFs being uniformly sampled from the space orthogonal to the harmonic oscillator ground state. Here we consider cases where we have 2 and 3 SPFs per mode.

mode we observe that none of the 1000 trajectories that were run fail to evolve according to the dominant optimal unoccupied SPF when using primitive Hilbert space dimension of up to 100. It is only for large primitive Hilbert space dimensions (10000), that an appreciable number of trajectories ($\sim 11\%$) follow the non-dominant solution. The average overlap of a randomly sampled vector in a D -dimensional space with an arbitrary vector in this space scales as D^{-1} . As such, for small local Hilbert space dimensions a randomly sampled vector will, on average, have a relatively large overlap with the dominant solution, and at least for this model will track the dominant solution.

As has previously been observed for the PSI,³⁶ when 3 SPFs are used per mode the dynamics becomes independent of the states of the initially unoccupied SPFs, and all trajectories track the two optimal unoccupied SPFs. This suggests that, at least for this model, the issues associated with the unoccupied SPFs are a result of insufficient convergence with respect to the number of SPFs. While

one of the unoccupied SPF provides the larger contribution to the dynamics initially, both contribute considerably to the dynamics, and as soon as there are enough SPFs to capture both important SPFs, the dependence on initial conditions entirely vanishes. As the number of SPFs increases towards a full Hilbert space calculation, the PSI is guaranteed to produce the correct result regardless of the initially unoccupied SPFs. Additionally, even when there are insufficiently many SPFs, this problem is unlikely to manifest unless specific poor choices of the initially unoccupied SPF are selected. Whether this holds true generally is outside of the scope of this work. However we do not observe issues related to the initially unoccupied SPFs in the following applications to models that are more representative of those that would be treated using ML-MCTDH based approaches.

B. Spin-Boson Model

The two-mode model treated in the previous section is not particularly representative of the types of models conventionally treated using ML-MCTDH. We now consider a number of larger problems, starting with a series of spin-boson models in which a single two-level system (TLS) is linearly coupled to a harmonic bath.^{46–49} The spin-boson Hamiltonian may be written as

$$\hat{H} = \varepsilon \hat{\sigma}_z + \Delta \hat{\sigma}_x + \hat{\sigma}_z \sum_k g_k (\hat{a}_k^\dagger + \hat{a}_k) + \sum_k \omega_k \hat{a}_k^\dagger \hat{a}_k, \quad (26)$$

where \hat{a}_k^\dagger and \hat{a}_k are the bosonic creation and annihilation operators associated with the k th bath mode, and

$$\hat{\sigma}_x = |0\rangle \langle 1| + |1\rangle \langle 0| \quad (27)$$

and

$$\hat{\sigma}_z = |0\rangle \langle 0| - |1\rangle \langle 1| \quad (28)$$

are Pauli matrices. The influence of the system on the bath is fully characterised by the bath spectral density^{47,49}

$$J(\omega) = \frac{\pi}{2} \sum_k g_k^2 \delta(\omega - \omega_k) \quad (29)$$

from which the system-bath coupling constants, g_k , and bath frequencies, ω_k , can be obtained. We will consider an Ohmic spectral density with an exponential cutoff

$$J(\omega) = \frac{\pi}{2} \alpha \omega e^{-\omega/\omega_c}, \quad (30)$$

where α is the dimensionless Kondo parameter and ω_c is the cutoff frequency of the bath.

An alternative representation of the spin-boson Hamiltonian can be obtained by applying the polaron transform⁴⁹

$$\hat{T} = \exp \left[-\hat{\sigma}_z \sum_k \frac{g_k}{\omega_k} (\hat{a}_k^\dagger - \hat{a}_k) \right], \quad (31)$$

which displaces the bath modes depending on the states of the TLS, to this Hamiltonian. The polaron-transformed spin-boson Hamiltonian can be written as

$$\begin{aligned}\hat{H}_{pol} &= \hat{T}^\dagger \hat{H} \hat{T} \\ &= \varepsilon \hat{\sigma}_z + \sum_k \omega_k \hat{a}_k^\dagger \hat{a}_k \\ &\quad + \left[\hat{\sigma}_+ \exp \left[-2 \sum_k \frac{g_k}{\omega_k} (\hat{a}_k^\dagger - \hat{a}_k) \right] + \text{h.c.} \right],\end{aligned}\quad (32)$$

in which the final term directly couples all bath and system modes in a multiplicative fashion. It has previously been shown that the polaron-transformed spin-boson model provides a considerably harder challenge for ML-MCTDH than the standard representation.^{2,3}

Before we can apply the PSI to simulating the unitary dynamics arising from either of these Hamiltonians, it is necessary to discretize the bath and consequently the spectral density. Following standard approaches,^{3,50} we will consider a discrete bath of N modes with system-bath coupling constant given by

$$g_k^2 = \frac{2 J(\omega_k)}{\pi \rho(\omega_k)}. \quad (33)$$

Here, $\rho(\omega)$ is the density of frequencies, which is taken to be

$$\rho(\omega) = \gamma e^{-\omega/\omega_c}, \quad (34)$$

with γ chosen to ensure correct normalization and the frequencies are given by

$$\int_0^{\omega_k} \rho(\omega) d\omega = k, \quad k = 1, 2, 3, \dots, N. \quad (35)$$

In the following discussion, we will consider the time-dependent population difference between the states of the two-level system as our observable of interest. This population difference is given by

$$P(t) = \langle \Psi(t) | \hat{\sigma}_z | \Psi(t) \rangle, \quad (36)$$

where the initial wavefunction is taken as

$$|\Psi(0)\rangle = |0\rangle \otimes |vac\rangle, \quad (37)$$

with $|vac\rangle$ denoting the vacuum state of the bath in the standard representation. Note here we only work at $T = 0$. Following Refs. 3 and 27, we will quantify the convergence of the population dynamics by using the relative cumulative deviation

$$\Delta P = \frac{1}{(P_{max} - P_{min})} \frac{1}{\tau} \int_0^\tau |P(t) - P_{ref}(t)| dt \quad (38)$$

from the population difference obtained from some reference calculation, $P_{ref}(t)$, obtained over a time period τ . Here, P_{min} and P_{max} are the minimum and maximum population differences throughout this time-period.

We will consider a relatively strongly coupled, unbiased ($\varepsilon = 0$) spin-boson model with $\alpha = 2$ and a cutoff frequency of $\omega_c = 25\Delta$. For all calculations here and in the Supplementary Information, the tree structure is constructed as follows. On the top layer, we consider $N_b + 1$ groups of SPFs, 1 of which accounts for the system degrees of freedom and contains a complete basis for the system (here this is 2 functions). The remaining N_b groups of SPFs treat the bath degrees of freedom, with the bath modes being partitioned between the groups so that they contain modes of similar frequencies. The bath SPFs in each of the N_b groups are then represented using as close to a balanced tree as possible with each node having up to N_{lower} SPF groups. Mode combination and adiabatic contraction are used for the bottom layer, with modes being grouped up to some maximum local Hilbert space.

Standard Representation

We will begin by considering a bath of $N = 500$ oscillators with $N_b = 2$ and $N_{lower} = 2$, and we will use 16 SPFs at each node in the bath subtrees. For each bath mode we will use a basis of 15 harmonic oscillator eigenfunctions and will allow for a maximum combined Hilbert space dimension of 3000. This will typically allow for 3 bath modes to be combined. We use an adaptive order, adaptive time step Lanczos integration scheme^{51,52} for integrating the linear systems of equations associated with each node, and in all calculations that follow we used an integration tolerance of 10^{-12} . In Table III of the Supplementary Information we consider the effect of varying this tolerance on the accuracy and efficiency of the simulations, and find that such a tolerance is more than sufficient to provide converged dynamics.

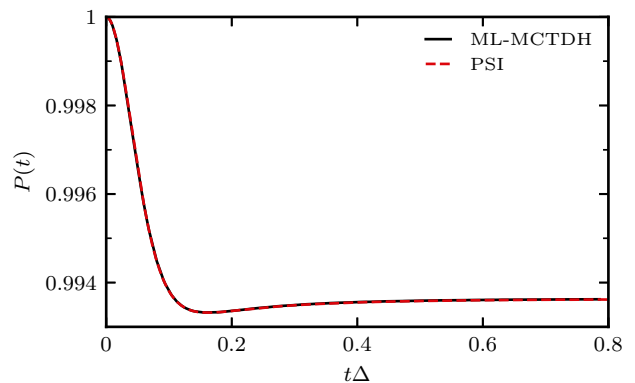


Figure 4. The time-dependent expectation value $P(t)$ obtained for a spin-boson model with $\varepsilon/\Delta = 0$, $\alpha = 2$, $\omega_c = 25\Delta$, and with $N = 500$ bath modes. Here the results obtained using the PSI are compared against the results obtained using the standard ML-MCTDH approach in Ref. 3.

The dynamics of $P(t)$ for this model has previously been obtained using standard ML-MCTDH and with the alternative regularization scheme mentioned in the introduction.³ In Fig. 4, we compare the results obtained using the PSI to their results in an effort to demonstrate the validity of our implementation of the PSI. Here we see population difference dynamics that agree well over the entire time period considered. Having validated our implementation of the multi-layer version of the PSI, we are now in a position to look at some more challenging cases.

Polaron-Transformed Representation

It has previously been shown that the standard ML-MCTDH approach fails to capture the dynamics of the polaron-transformed representation of the spin-boson model.^{2,3} This is due to the inability of the regularized ML-MCTDH EOMs to accurately capture the rapid evolution of unoccupied SPFs required for this representation, and an alternative regularization scheme is required to obtain accurate dynamics.^{2,3} In panel a) of Fig. 5, we present the dynamics of the polaron-transformed representation of the spin-boson model considered in Fig. 4 obtained using the PSI with a range of constant time steps.

The population dynamics obtained for the polaron-transformed Hamiltonian converges considerably slower than the population dynamics obtained when using the standard representation (shown in Fig. 4). By considering the time-dependent deviation from the reference calculation shown in the inset of panel a) of Fig. 5, it can be seen that the significant deviation observed is dominated by errors made in the first time step, following which the deviation from the reference calculations reaches a plateau. In order to accurately describe the dynamics of this Hamiltonian, and in particular the contribution arising from the final term in Eq. 32 that couples all modes to all other modes in a multiplicative manner, the SPFs need to undergo rapid evolution. Within the PSI, the coefficients for each node are evolved over each time period with the SPFs held constant. When the SPFs evolve rapidly, this provides a poor approximation to the true dynamics, as the full evolution operator quickly leaves the region of the Hilbert space described by the constant SPF and SHF basis. As such, in contrast to the standard ML-MCTDH approach where numerical issues arise from difficulties in describing this rapid evolution of SPFs, the deviations observed for the PSI can be attributed to errors associated with the constant mean-field approximation.

In order to demonstrate this point, we consider an alternative integration scheme in which the initial evolution through the interval dt is split into a series of smaller time steps, with each time step being an order of magnitude larger than the previous until we reach time $t = dt$ (i.e. if 5 steps are used the first uses a time step of $10^{-5}dt$). The

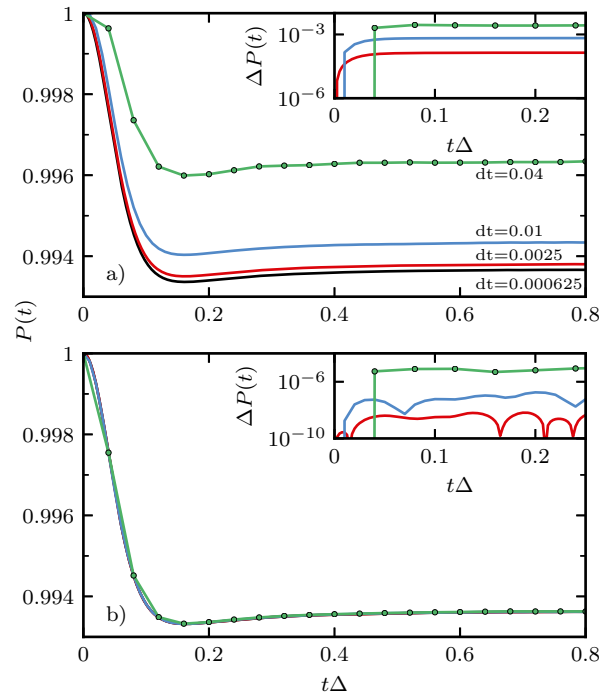


Figure 5. The effect of time step on the convergence of $P(t)$ for a polaron-transformed spin-boson model with $\varepsilon/\Delta = 0$, $\alpha = 2$, $\omega_c = 25\Delta$, and with $N = 500$ bath modes. a) Results obtained using a fixed time step integrator (with time steps shown). b) Results alternative scheme that makes use of a series of smaller time steps to integrate from $t = 0$ to $t = dt$ but uses the same fixed step as in panel a) for all times $t > dt$. The insets in each panel show the absolute difference of the results obtained with a given time step and the reference calculation obtained with $dt\Delta = 0.000625$.

results obtained using this scheme are shown in panel b) of Fig. 5. With this modification to the integration protocol, we see a three orders of magnitude reduction in the deviation of the population dynamics even for a time step of $dt\Delta = 0.04$, and as a consequence the population dynamics converges more rapidly in this case than for the standard spin-boson model.

These results suggest that the PSI is readily able to accurately capture rapid evolution of the initially unoccupied SPFs. In addition, this approach can benefit from an adaptive time step integration scheme. The error associated with the PSI can vary significantly throughout a simulation depending on how rapidly the SPF and mean-field Hamiltonian matrices evolve. In principle, an adaptive time step integration scheme would resolve this issue.

We have applied the adaptive integration approach described in Ref. 36 for the MCTDH case to the multi-layer case. This scheme involves propagating two approximations to the ML-MCTDH wavefunction obtained using time steps that differ by a factor of two, and as such allows for an estimate of the error of the integration to be obtained. However, we find that due to a build-up

of floating point errors in the evaluation of the Hilbert angle (or overlap) between the two approximations of the wavefunction used in this approach, the error estimate itself has limited accuracy for deep tree structures ($\sim 10^{-6}$). This approach provides a reasonable adaptive integration scheme when moderate integration errors are allowed ($\sim 10^{-5}$), however, for problems requiring stricter tolerances we find that such an approach often becomes impractical as it is unable to accurately estimate the error.

Dependence on Initially Unoccupied SPFs

We next consider the dependence of the dynamics obtained for the model with different choices for the initially unoccupied SPFs. To do this we perform a series of simulations with different initially unoccupied SPFs. For each node in the tree, we sample the coefficients of the unoccupied SPF uniformly within the local Hilbert space such that they are orthogonal to our initially occupied state. We run a series of 20 different simulations for both the standard and polaron-transformed spin-boson model with $N = 500$ bath modes, and consider the average relative cumulative deviation over the 20 trajectories taking the mean of all trajectories as the reference. The resultant mean deviations are given in Table II. Some de-

$dt\Delta$	$\langle\Delta P\rangle$: Standard	$\langle\Delta P\rangle$: Polaron
4×10^{-2}	1.9×10^{-3}	3.0×10^{-4}
2×10^{-2}	9.7×10^{-5}	4.7×10^{-5}
1×10^{-2}	1.0×10^{-5}	4.9×10^{-6}
5×10^{-3}	3.8×10^{-6}	1.2×10^{-6}
2.5×10^{-3}	1.5×10^{-6}	1.6×10^{-6}
1.25×10^{-3}	2.5×10^{-7}	1.3×10^{-6}
6.25×10^{-4}	8.5×10^{-8}	1.7×10^{-6}

Table II. Average cumulative deviation of 20 simulations from their mean obtained with different initially unoccupied SPFs.

viations in the population dynamics obtained with different initially unoccupied SPFs are observed. For larger time steps, these relative deviations can be rather large, on the order of 10^{-3} . As the time step is decreased, the mean deviations likewise decrease, and converge towards the results shown in Fig. 4. For this problem, the choice of the redundant initial conditions does not significantly impacts the dynamics obtained provided they are converged with respect to the integration time step.

Larger Bath Sizes

Finally, for this model, we explore the effect that increasing the number of bath modes has on the accuracy and efficiency of the dynamics obtained using the PSI. We consider a series of six bath sizes ranging from 500 to 10^6 modes and treat the dynamics using the standard representation for the Hamiltonian. We once again use

the relative deviation with respect to a reference calculation for each bath size as a measure of the accuracy, and use the total number of Hamiltonian evaluations, N_{MF} , and average number of Hamiltonian applications per node, $\langle N_H \rangle$, as measures of efficiency. For variable mean-field based approaches, such as those considered in Refs. 3 and 27, these two quantities are the same where as for the PSI they can differ. Depending on the specific application, either of these two steps can dominate the numerical cost associated with the calculation. For all calculations we used the alternative integration scheme introduced in the previous section, and the approach outlined above for constructing the tree topology. For all trees we use 16 SPFs per node for the first nine layers of nodes (or as many layers as the tree has), and four SPFs per node for all other nodes. This corresponds to a similar tree structure to that used for this model in Ref. 27, and is sufficient to converge the dynamics with respect to the number of SPFs. In Table III, the convergence behavior of the PSI is compared for baths with 500, 2,000, 5,000, 10^4 , 10^5 , and 10^6 modes. For all bath sizes, convergence of the population dynamics (here taken to be a deviation of $\sim 10^{-4}$) is observed for time steps of $dt\Delta = 1 \times 10^{-2}$ or smaller. As the number of bath modes increases, the average number of Hamiltonian applications required decreases slightly. However, this decrease is not particularly significant and can likely be attributed to the tree structure used. For problems with large numbers of bath modes we have a considerably larger proportion of nodes that use four SPFs rather than sixteen SPFs. For these nodes the solution of Eq. 9 using a Krylov subspace integration scheme requires slightly fewer function applications although this difference decreases as the time step decreases. For all bath sizes this corresponds to a total of 170 Hamiltonian evaluations and with $\lesssim 2 \times 10^3$ average Hamiltonian applications per node. In comparison, standard ML-MCTDH calculations require roughly three to four orders of magnitude more mean-field evaluations and two to three orders of magnitude more Hamiltonian evaluations to obtain the same error for baths of up to 10^4 modes.^{3,27} The difference in efficiency is less extreme when compared to the improved regularization scheme presented in Ref. 3, however even in this case the PSI requires roughly 30-80 times fewer Hamiltonian evaluation and 3-8 times fewer Hamiltonian applications for baths of up to 10^4 modes. This difference becomes more pronounced when considering the 10^5 mode case. For the PSI, the number of Hamiltonian evaluations and applications required for convergence is essentially independent of the number of bath modes. For the improved regularization scheme results presented in Ref. 27, a factor of 10 increase in the number of evaluations required is observed when moving from 10^4 to 10^5 modes. For reference, the PSI calculations for the 10^5 mode model using a time step of $dt\Delta = 1 \times 10^{-2}$ required less than three hours on a single core of an Intel i5-8250U CPU.

These results suggests that for the PSI the number

N	500			2,000			5,000		
$dt\Delta$	N_{MF}	ΔP	$\langle N_H \rangle$	ΔP	$\langle N_H \rangle$	ΔP	$\langle N_H \rangle$		
4×10^{-2}	50	1.6×10^{-2}	9.9×10^2	9.4×10^{-3}	8.6×10^2	1.3×10^{-2}	8.0×10^2		
2×10^{-2}	90	1.6×10^{-4}	1.4×10^3	1.3×10^{-4}	1.3×10^3	2.2×10^{-4}	1.1×10^3		
1×10^{-2}	170	1.2×10^{-5}	2.1×10^3	2.3×10^{-5}	1.9×10^3	1.6×10^{-5}	1.7×10^3		
5×10^{-3}	330	5.0×10^{-6}	3.2×10^3	2.3×10^{-6}	2.9×10^3	3.2×10^{-6}	2.7×10^3		
2.5×10^{-3}	650	3.4×10^{-6}	5.3×10^3	8.1×10^{-7}	4.9×10^3	7.1×10^{-7}	4.6×10^3		
1.25×10^{-3}	1290	1.8×10^{-7}	9.3×10^3	2.5×10^{-7}	8.8×10^3	2.1×10^{-7}	8.3×10^3		
6.25×10^{-4}	2570	Reference	1.7×10^4	Reference	1.6×10^4	Reference	1.5×10^4		

N	10^4			10^5			10^6		
$dt\Delta$	N_{MF}	ΔP	$\langle N_H \rangle$	ΔP	$\langle N_H \rangle$	ΔP	$\langle N_H \rangle$		
4×10^{-2}	50	1.6×10^{-2}	7.5×10^2	1.2×10^{-2}	6.7×10^2	1.4×10^{-2}	5.3×10^2		
2×10^{-2}	90	5.1×10^{-4}	1.0×10^3	4.1×10^{-4}	9.5×10^2	3.0×10^{-4}	8.0×10^2		
1×10^{-2}	170	1.5×10^{-5}	1.6×10^3	1.6×10^{-5}	1.4×10^3	1.7×10^{-5}	1.3×10^3		
5×10^{-3}	330	2.6×10^{-6}	2.5×10^3	2.3×10^{-6}	2.4×10^3	4.2×10^{-6}	2.2×10^3		
2.5×10^{-3}	650	3.9×10^{-7}	4.4×10^3	5.8×10^{-7}	4.1×10^3	1.3×10^{-6}	4.0×10^3		
1.25×10^{-3}	1290	1.0×10^{-7}	8.1×10^3	2.7×10^{-7}	7.7×10^3	8.6×10^{-7}	7.4×10^3		
6.25×10^{-4}	2570	Reference	1.5×10^4	Reference	1.4×10^4	Reference	1.3×10^4		

Table III. The convergence with respect to time step (dt) of the deviation in the population dynamics of a spin-boson model obtained using the PSI. The spin-boson model considered has $\varepsilon/\Delta = 0$, $\alpha = 2$, $\omega_c = 25\Delta$, and with varying numbers of bath modes (specified in the tables). In all cases, the dynamics was obtained using the alternative integration scheme described above and the relative cumulative deviation (from the indicated reference) was evaluated for dynamics obtained to times $t\Delta = 0.8$.

of Hamiltonian evaluations and applications at a given time step is limited by the physics of the problem, and as the number of bath modes increases, little change in the number of these operations occurs. For ML-MCTDH approaches that employ regularized EOMs, the required regularization parameter depends on the number of bath modes and as a consequence considerably more integration steps are required to obtain converged results for larger baths.

All calculations presented in this section have used a relatively deep tree structure. In contrast, the results obtained in Refs. 3 and 27 for this model with bath sizes up to $N = 10^4$ were obtained using wider trees. In Table V of the Supplementary Information, we present results obtained using wider tree structures generated with $N_b = 4$ or 5, and $N_{lower} = 4$. We find that the conclusions reached in this section do not change when using this alternative tree topology, and thus the accuracy and efficiency when measured in terms of the number Hamiltonian applications and Hamiltonian evaluations of the PSI does not depend significantly on the tree structure. In addition to these results, we have considered the full set of spin-boson models considered in Ref. 3. For completeness these results are presented in Sec. VII of the Supplementary Information, and once again the PSI can obtain converged results with roughly 1-2 orders of magnitude fewer Hamiltonian evaluations and comparable to an order of magnitude fewer Hamiltonian applications than the improved regularization approach.

For all of the calculations presented so far, relatively few SPFs are required to obtain converged results, and as such do not represent particularly challenging problems. We will now consider a significantly more challeng-

ing physical system for which considerably more SPFs are required in order to obtain accurate dynamics.

C. Multi-Spin-Boson Model

As a final application of the PSI approach we consider a generalization of the spin-boson model, in which a set of M TLSs are each linearly coupled to a *common* harmonic oscillator bath. The Hamiltonian for this system may be written as

$$\hat{H} = \sum_{i=1}^M (\varepsilon \hat{\sigma}_{i,z} + \Delta \hat{\sigma}_{i,x}) + \sum_k \omega_k \hat{a}_k^\dagger \hat{a}_k + \sum_{i=1}^M \hat{\sigma}_{i,z} \sum_k g_{ik} (\hat{a}_k^\dagger + \hat{a}_k), \quad (39)$$

where \hat{a}_k^\dagger and \hat{a}_k are the bosonic creation and annihilation operators associated with the k th bath mode, and $\hat{\sigma}_{i,x}$ and $\hat{\sigma}_{i,z}$ are the Pauli matrices associated with spin i . Eq. 39 provides an interesting model in which to explore the interplay between coherent system interactions and the effects of dissipation arising from the bath.⁵³⁻⁵⁶ For Ohmic and sub-Ohmic baths, the presence of the additional TLSs have been shown to enhance localization, reducing the system-bath coupling strength at which the delocalization to localization transition occurs.⁵³⁻⁵⁶ Additionally, the model with a super-Ohmic bath arises in the description of low temperature glasses,⁵⁷⁻⁶⁰ where it has been suggested that signatures of many-body localization may be experimentally observable.⁶⁰ In what follows, we will restrict ourselves to the case of an Ohmic

bath. In contrast to the standard spin-boson model, where the influence of the bath on the system is entirely encoded within the spectral density, the MSB model involves an $M \times M$ matrix of spectral densities. The elements of this matrix of spectral densities, are given by

$$J_{ij}(\omega) = \frac{\pi}{2} \sum_k g_{ik} g_{jk} \delta(\omega - \omega_k) \quad (40)$$

and can be used to specify the system-bath coupling constants, g_{ik} , between spin i and mode k , and the frequency of mode k , ω_k . We will consider diagonal spectral densities that are Ohmic with an exponential cutoff

$$J_{ii}(\omega) = \frac{\pi}{2} \alpha \omega e^{-\omega/\omega_c}, \quad (41)$$

and off-diagonal spectral densities of the form⁵⁵

$$J_{ij}(\omega) = \frac{\pi}{2} \alpha \omega e^{-\omega/\omega_c} \cos(\omega r_{ij}/\nu), \quad (42)$$

where α is the dimensionless Kondo parameter, ω_c is the cutoff frequency of the bath, $r_{ij} = |x_i - x_j|$ is the distance between the TLSs i and j , and ν is the speed of sound in the bath. As a result of this cosine term, the peak in the off-diagonal bath correlation functions is delayed compared to the diagonal correlation functions to time $t = \tau_{ij} = r_{ij}/\nu$. This gives rise to inherently non-Markovian phonon-mediated interactions between TLSs. This form for the spectral density matrix arises when considering a set of TLSs coupled to a common one-dimensional bath of phonons.⁵⁵

In order to perform simulations of the unitary dynamics of this system, it is necessary to discretize the bath. As in the single spin-boson case we have used an exponential density of bath frequencies (Eq. 34), and have discretized the bath into a set of N frequencies according to Eq. 35. For each of mode, there is a set of M coupling constants that need to be determined. These coupling constants need to satisfy the set of $M \times M$ equations for the spectral densities. If all TLSs are not at the same position in space, it is not possible to satisfy all equations with a single set of M coupling constants. Rather we consider a set of M modes, each with the same frequency, that each couple to all the TLSs. This gives us an $M \times M$ matrix of coupling constants, \mathbf{g}_k , for each frequency that needs to satisfy the equation

$$\mathbf{g}_k^T \mathbf{g}_k = \frac{2}{\pi} \frac{\mathbf{J}(\omega_k)}{\rho(\omega_k)}, \quad (43)$$

where $\mathbf{J}(\omega)$ is the matrix of spectral densities. Here we construct a symmetric matrices of coupling constants \mathbf{g}_k by taking the principal square root of the right hand side. Applying this process, we arrive at a bath of $N \times M$ modes, with M distinct frequencies.

We will consider a series of MSB models with up to six TLSs, with randomly sampled positions, all coupled to the same bath. We choose parameters such that the

$\frac{\epsilon_i/\Delta}{0}$	$\frac{\Delta_i/\Delta}{1}$	$\frac{\alpha}{2}$	$\frac{\omega_c/\Delta}{2.5}$		
$\frac{x_1\Delta/\nu}{2.08463}$	$\frac{x_2\Delta/\nu}{4.59884}$	$\frac{x_3\Delta/\nu}{4.73564}$	$\frac{x_4\Delta/\nu}{4.62870}$	$\frac{x_5\Delta/\nu}{2.39182}$	$\frac{x_6\Delta/\nu}{0}$

Table IV. MSB model parameters used in the calculations performed in this section. All parameters are defined with respect to the Tunnelling amplitude, Δ , which specifies the energy scales involved. As only the relative positions are important, the positions of the TLS, x_i , have been shifted from their randomly sampled values.

timescales associated with the bath dynamics are comparable to the timescales of the TLS dynamics, the physical parameters used are shown in Table IV.

In the following calculations we will evaluate the dynamics of the time-dependent population difference for each TLS,

$$P_i(t) = \langle \Psi(t) | \hat{\sigma}_{i,z} | \Psi(t) \rangle, \quad (44)$$

where the initial wavefunction is taken to be

$$|\Psi(0)\rangle = \bigotimes_{i=1}^M |0\rangle_i \otimes |vac\rangle. \quad (45)$$

We will measure the convergence of this dynamics by looking at the average relative deviation obtained for the population dynamics of each of the TLSs

$$\langle \Delta P \rangle = \frac{1}{M} \sum_{i=1}^M \frac{1}{(P_{i,max} - P_{i,min})} \frac{1}{\tau} \int_0^\tau |P_i(t) - P_{i,ref}(t)| dt, \quad (46)$$

where $P_{i,ref}(t)$ is a reference result for the population dynamics of TLS i , and $P_{i,min}$ and $P_{i,max}$ are the minimum and maximum values of population difference.

Convergence with Respect to N_{SPF}

We have considered the dynamics of four different MSB models with $M = 1, 2, 4,$ and 6 TLSs. The bath is discretized using 512 distinct frequencies, and as a consequence baths of 512, 1024, 3048, and 3072 modes are used for the 1, 2, 4, and 6 TLSs systems, respectively. The ML-MCTDH wavefunctions used in these calculations employed three groups of SPFs at the top level, one of which accounts for the degrees of freedom of the TLSs and includes as many SPFs as there are functions in the multi-TLS Hilbert space (2^M). The remaining two groups accounted for the bath degrees of freedom. The partitioning of bath modes uses the same procedure as used above for the spin-boson model, and employed two SPF groups for all subsequent layers. Simulations were performed with a range of different numbers of SPFs for treating the bath degrees of freedom, N_{spf} , however, in all cases twice as many functions ($2N_{spf}$) were used for

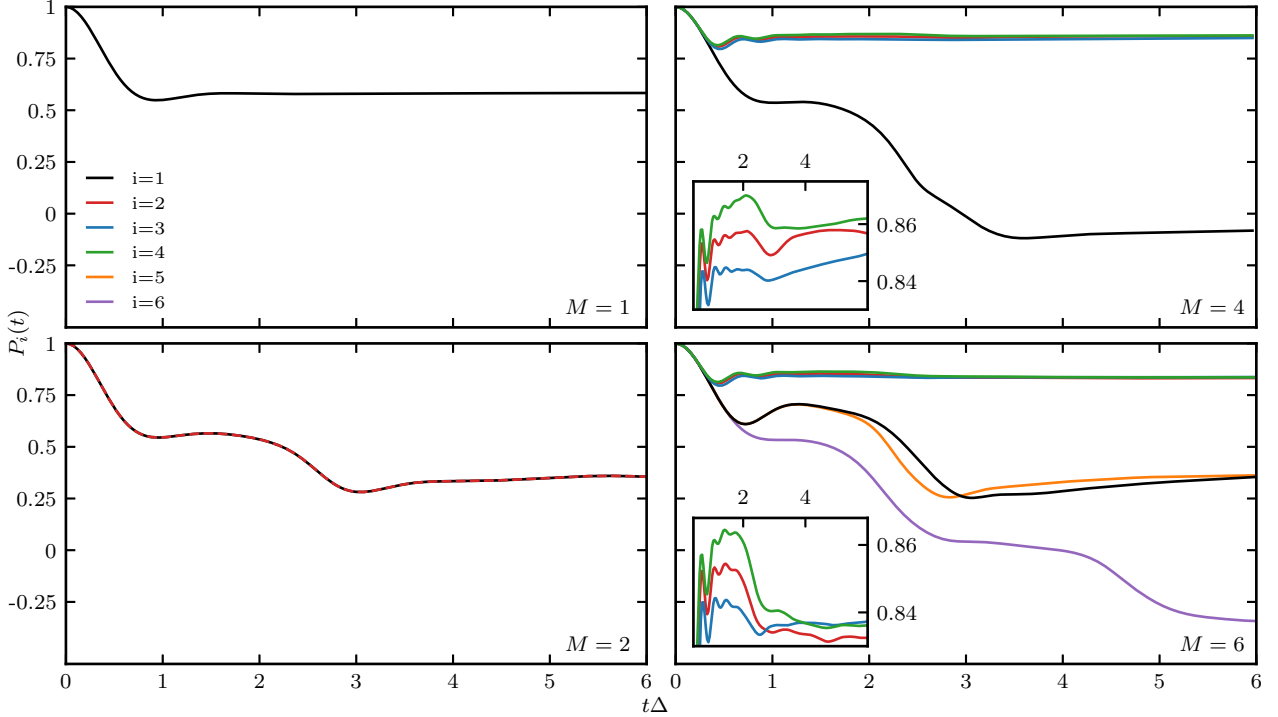


Figure 6. Population dynamics for each of the TLSs in a series of MSB models with varying numbers of TLSs coupled to a common heat bath. A bath containing 512 distinct frequencies is used in each case which correspond to baths containing 512, 1024, 2048, and 3072 bath modes for 1,2,4, and 6 TLSs, respectively. The inlays for the 4 and 6 spin cases, provide a closeup of the population dynamics for TLSs 2,3, and 4 all of which are located in a similar point in space.

the root node. The largest calculations considered here used $N_{spf} = 100$. For the system with six TLSs this corresponds to expanding the wavefunction in terms of a basis of $2^6 \times 200^2 = 2,560,000$ states at the top layer, and $100^3 = 1,000,000$ basis states for all other non-leaf layers. A total of $\sim 1.3 \times 10^9$ variational parameters were used to parameterize the wavefunction. A primitive basis of 30 harmonic oscillator basis functions is used for each leaf node with frequency less than the bath cutoff frequency and 10 basis functions for all higher frequency modes. Mode combination was used with multiple physical modes being combined together up until a maximum Hilbert space dimension of 3000 was reached. All calculations presented in this section were performed with a time step of $dt\Delta = 0.04$, unless otherwise specified, which was found sufficient to provide results converged to a relative cumulative deviation of $\sim 10^{-5}$.

The results used as the reference calculations for each of the different MSB models are shown in Fig. 6. These calculations used $N_{spf} = 48, 80, 100,$ and 100 for $M = 1, 2, 4,$ and 6 TLSs, respectively. The dynamics obtained for the one TLS case are not particularly interesting; we see rapid initial decay of the population difference following which it plateaus to a finite value as the system is at sufficiently strong coupling that the dynamics are within the localised phase. For the two TLSs case, the population dynamics obtained for each TLS is identical

due to symmetry. For short times the dynamics closely resembles that of the single TLS case, however, starting at around $t\Delta \sim 2.5$ the population difference begins to decay further before reaching a lower plateau at later times. This corresponds to the time required for propagation of phonons between the two TLSs, and so this further decay arises due to phonon mediated interactions between the TLSs. For the four and six TLSs cases, the population dynamics of TLSs 2, 3, and 4 are very similar (as shown in the insets). This arises due to the close proximity of these TLSs and thus the timescale on which the bath induces coupling between these TLSs is considerably faster than the timescale of the bath dynamics. In this regime, the bath-mediated interactions can be well described by a relatively strong, ferromagnetic, $\hat{\sigma}_{i,z}\hat{\sigma}_{j,z}$ coupling between the TLSs that results in strong correlations between the dynamics of these spins. At later times, these TLSs interact with the other TLSs present, and can result in significant changes in the population dynamics of the other spins due to the cumulative effect of the three spins.

In order to accurately capture the dynamics of these systems, it is necessary to have enough SPFs that the correlations between individual TLSs and bath as well as the bath-mediated correlations between the TLSs can be well described. This becomes a more challenging problem as the number of TLSs increase, and as a result we find that

M	1		2		4		6	
N_{spf}	$\langle \Delta P \rangle$	$\langle N_H \rangle$	$\langle \Delta P \rangle$	$\langle N_H \rangle$	$\langle \Delta P \rangle$	$\langle N_H \rangle$	$\langle \Delta P \rangle$	$\langle N_H \rangle$
4	3.5×10^{-3}	2.2×10^3	1.7×10^{-1}	2.1×10^3	1.2×10^{-1}	2.4×10^3	1.4×10^{-1}	2.4×10^3
8	3.8×10^{-4}	2.4×10^3	8.7×10^{-3}	2.3×10^3	5.5×10^{-2}	2.5×10^3	5.5×10^{-2}	2.5×10^3
12	4.0×10^{-5}	2.5×10^3	3.7×10^{-3}	2.3×10^3	3.0×10^{-2}	2.5×10^3	7.7×10^{-2}	2.5×10^3
16	8.1×10^{-6}	2.5×10^3	3.7×10^{-3}	2.4×10^3	2.4×10^{-2}	2.6×10^3	3.9×10^{-2}	2.5×10^3
24	2.7×10^{-6}	2.6×10^3	4.8×10^{-4}	2.6×10^3	1.0×10^{-2}	2.6×10^3	2.6×10^{-2}	2.7×10^3
32	1.3×10^{-6}	2.7×10^3	3.0×10^{-4}	2.6×10^3	6.0×10^{-3}	2.7×10^3	1.7×10^{-2}	2.6×10^3
48	Reference	3.8×10^3	4.9×10^{-5}	2.7×10^3	2.1×10^{-3}	3.2×10^3	1.1×10^{-2}	2.6×10^3
64			2.4×10^{-5}	2.8×10^3	1.5×10^{-3}	3.3×10^3	7.0×10^{-3}	2.7×10^3
80			Reference	2.9×10^3	7.1×10^{-4}	2.7×10^3	3.3×10^{-3}	2.7×10^3
100					Reference	3.3×10^3	Reference	2.7×10^3

Table V. Convergence of the population dynamics obtained for the MSB models with varying numbers of TLSs, M , as a function of the number of SPFs, N_{spf} . Convergence is measured through the average relative deviation of the population dynamics from reference calculations indicated in the table. We also present the average number of Hamiltonian evaluations per node required to obtain this dynamics out to a time $t\Delta = 6$.

significantly more SPFs are required to obtain accurate dynamics. In Table V we present the average relative deviations of the population dynamics of the systems and number of Hamiltonian applications required for varying numbers of SPFs. The number of Hamiltonian applications required for a given number of SPFs appears to be roughly independent of the number of TLSs considered. However there is a trend of requiring more Hamiltonian applications as the number of SPFs increases. This dependence is not very strong, with at most a factor of 2 increase being observed. As such, the increase in the number of Hamiltonian applications does not dramatically impact the computational effort associated with the calculations as the number of SPFs increase. It would be interesting to see whether this holds for the standard ML-MCTDH approach and improved schemes that employ regularization of singular mean-field density matrices. Whether the increase in the size of these mean-field density matrices due to an increase in the number of SPFs alters the size of the regularization parameter required to obtain converged results is not immediately obvious. Furthermore, whether the larger number of initially unoccupied SPFs increases the time over which the regularization impacts the dynamics remains to be seen.

The convergence of the population dynamics with respect to the number of SPFs differs considerably for systems with different numbers of TLSs. For the single TLS (spin-boson model) case, convergence is very rapid with deviations $< 10^{-4}$ being obtained for $N_{spf} \geq 12$. As the number of TLSs increase it becomes considerably more challenging to converge dynamics. For the two TLSs case, a deviation $< 10^{-4}$ is not obtained until $N_{spf} \geq 48$. Whereas for the four and six TLSs case, the deviations between the population dynamics obtained for the largest numbers of SPFs ($N_{spf} = 80$ and 100) are 7.1×10^{-4} and 3.3×10^{-3} , respectively. These relatively large deviations indicate that the dynamics are not fully converged with respect to the number of SPFs used. To give a more clear indication of the scale of these deviations, the population dynamics obtained for the four and six TLS models using

$N_{spf} = 64, 80,$ and 100 are shown in Fig. 7.

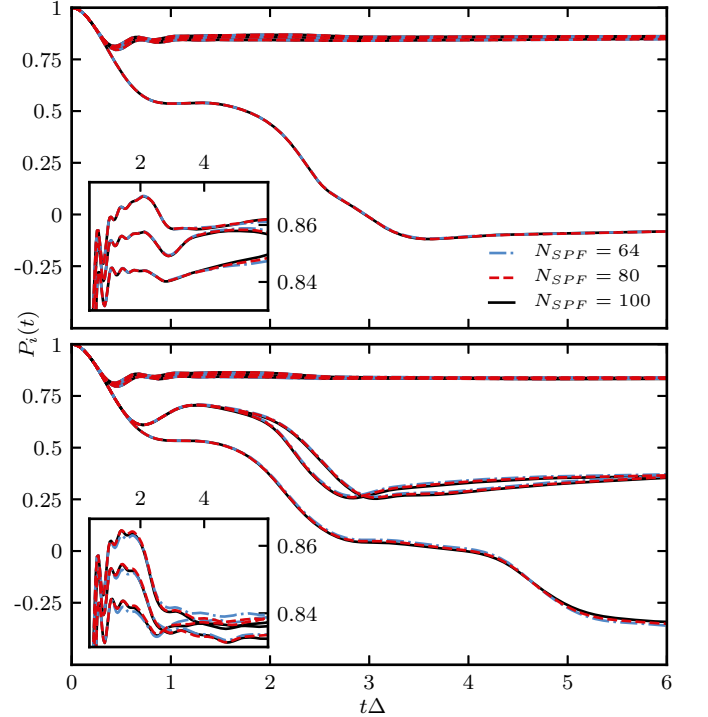


Figure 7. Convergence of the population dynamics with respect to the number of SPFs for $M = 4$ (top) and 6 (bottom) TLSs. The population difference as a function of time for each TLS is shown. In each case, results were obtained using $N_{spf} = 64, 80,$ and 100 SPFs. The insets show a zoomed in view of the population difference dynamics for spins 2,3, and 4, which experience similar population dynamics.

For the four TLSs case, the population dynamics are converged to within the thickness of the lines shown when represented on the larger scale, however, some small deviations are observed in the population dynamics of TLSs 2,3, and 4 at times $t\Delta \geq 4$ (shown in the insets). For

many applications, this level of convergence is sufficient. For the six TLSs case, more significant deviations are observed between the results with different numbers of SPFs, with the onset of these significant deviations being at shorter times $t\Delta \geq 1.5$. The timescale of the dynamics of TLSs 1, 5, and 6 is not fully converged, with the $N_{spf} = 100$ case showing a slight shift to shorter times. In both cases, the results obtained with $N_{spf} = 80$ agree with the results obtained using $N_{spf} = 100$ to longer times than the results obtained $N_{spf} = 64$, and show smaller deviations once they occur. In order to obtain fully converged results it would be necessary to consider even larger number of SPFs than have been considered here.

The primary factor limiting the number of SPFs that can be treated is the $\mathcal{O}(N_{spf}^4)$ scaling of operations at each node, and $\mathcal{O}(N_{spf}^3)$ scaling of the memory requirements. For reference, the six TLSs calculations with $N_{spf} = 100$, required ~ 32 GB of memory to store the required data for the evolution. The memory limitations can be offset significantly through the use of out-of-core storage techniques. However, even with such techniques the size of systems that are practical to treat are still limited by the $\mathcal{O}(N_{spf}^4)$ scaling of the number of operations applied to each node. The serial updating of nodes within the PSI limits the extent to which it can be parallelized. Only the linear algebra kernels applied in the evolution of each node can readily be parallelized. As a consequence, the wall time requirements can become very large for systems with larger numbers of SPFs. For reference, the six TLSs calculations with $N_{spf} = 100$ took ~ 480 hours running on 8 cores of an Intel Xeon E5-2690 v3 CPU. For this case the speed up due to the use of parallelized linear algebra kernels was sublinear. However, it is likely that with further optimization better parallel performance could be obtained. This poor parallel performance arising from the serial nature of the node updates represents one of the main limitations of the current PSI approach.

Effect of Varying Timestep

As the number of SPFs increase, the deviation between results obtained with a given time step and the reference calculation obtained with a time step of $dt\Delta = 5 \times 10^{-3}$ decreases significantly. This result is readily understood when considering the approximations involved in obtaining the PSI. The PSI uses an expansion of the full wavefunction in terms of an orthonormal basis at each node of the tree. The evolution of the coefficient tensor at each node involves the construction of the propagator obtained from the projection of the Hamiltonian onto this local basis. As the size of this local basis increases, the projection of the Hamiltonian onto this basis better approximates the Hamiltonian in the full Hilbert space, and as a consequence the propagator evaluated using this projected Hamiltonian is accurate for longer times, and

N_{spf}	4	16	32	48
$dt\Delta$	$\langle \Delta P \rangle$			
6.4×10^{-1}	3.5×10^{-2}	6.7×10^{-3}	1.1×10^{-3}	4.6×10^{-4}
3.2×10^{-1}	1.6×10^{-2}	1.2×10^{-3}	2.4×10^{-4}	7.1×10^{-5}
1.6×10^{-1}	5.0×10^{-3}	5.6×10^{-4}	7.6×10^{-5}	1.4×10^{-5}
8×10^{-2}	2.5×10^{-3}	4.5×10^{-4}	5.3×10^{-5}	4.9×10^{-6}
4×10^{-2}	5.1×10^{-4}	4.0×10^{-4}	3.1×10^{-5}	4.4×10^{-6}
2×10^{-2}	2.8×10^{-4}	8.5×10^{-4}	3.2×10^{-5}	4.0×10^{-6}
1×10^{-2}	1.3×10^{-4}	5.4×10^{-4}	1.8×10^{-5}	2.1×10^{-6}
5×10^{-3}	Reference	Reference	Reference	Reference

Table VI. Convergence of the population dynamics of the two TLS model with respect to time step for different numbers of SPFs. In each calculation the model parameters are as given in the main text. For each value of N_{spf} , convergence is measure with respect to a different reference, the calculation obtained with that value of N_{spf} and with a time step of $dt\Delta = 5 \times 10^{-3}$.

fewer Hamiltonian evaluations are required when integration the equations. In the limit of a complete basis expansion at each node of the tree, the propagator becomes exact and the approximation of a constant mean-field becomes exact for arbitrary times. These results further suggest that the projector splitting integrator could benefit significantly from an adaptive time step integration scheme. In particular, as the number of SPFs is increased such a scheme would be able to take larger time steps, potentially reducing the computational effort required to obtain converged results.

There is one additional point that we need to consider when discussing the convergence of the dynamics of this model. In principle, the dynamics should be converged with respect to the number of discrete bath modes, M , in order to reach the continuum bath limit. The memory and computer time requirements scale as $\mathcal{O}(M \log(M))$. Here, due to the large wall time requirements necessary to perform the calculations with large tree sizes and large number of SPFs we have restricted the bath to only 512 frequencies for the four and six TLSs cases. For the one and two TLSs cases, calculations using larger baths are feasible and are shown in Sec. VII.A of the Supplementary Information. Finally, as in the spin-boson model case, it is possible to perform a polaron transform for the MSB model. We have considered this in Sec. VII.B of the Supplementary Information for the one and two TLSs cases. These results show that, once again, the PSI has no issue when treating the challenging polaron-transformed representation.

IV. CONCLUSION

In this paper we have discussed the implementation of the PSI for ML-MCTDH wavefunctions and have presented a series of numerical applications. Here, we have consider three different types of models:

- A two-dimensional, bi-linearly and bi-quadratically

coupled harmonic oscillator model.

- A series of spin-boson models using both the standard and polaron-transformed forms of the Hamiltonian.
- A series of multi-spin-boson models.

These three types of models have allowed us to explore the stability and efficiency of the PSI in a number of different regimes.

The two-dimensional oscillator model serves as a useful test for how rank deficiency in the ML-MCTDH wavefunction influences the accuracy of the dynamics obtained by the PSI. The dynamics of unoccupied SPFs is arbitrary within any dynamical method that is based on linear variations, such as standard ML-MCTDH or the PSI. As a consequence, the dynamics of the wavefunction can depend on the value chosen for these unoccupied SPFs that do not initially contribute to the wavefunction. Here we find that while the dynamics obtained for this two-dimensional model can depend on the value of the initially unoccupied SPFs when 2 SPFs are used, uniformly sampling the initially unoccupied SPFs typically leads to dynamics that corresponds to the optimal choice of the initially unoccupied SPF. Further, if we increase the number of SPFs used to 3, then the results obtained do not depend on the initial choice of these functions. It is only when we have insufficient flexibility in the wavefunction to account for the two unoccupied SPFs that contribute significantly to the dynamics at short times that we find this dependence on initial conditions. While this two-dimensional model provides a convenient test case for the behavior of unoccupied SPFs it is not representative of the types of problems that ML-MCTDH would typically be applied to.

We next considered a series of spin-boson models that more closely resemble the types of problems that are typically treated using ML-MCTDH, and allow us to observe how the PSI performs for problems with considerably more modes. Converged dynamics were obtained for systems with up to 10^6 degrees of freedom represented using tree structures with $\mathcal{O}(10^5)$ nodes. By comparison with results that have previously been obtained using standard ML-MCTDH (and an improved variant) for systems with fewer modes,^{3,27} we find that the PSI approach provides an efficient and accurate approach. When compared to standard ML-MCTDH, we find that the PSI approach required between 3-4 orders of magnitude fewer Hamiltonian evaluations and 2-3 orders of magnitude fewer Hamiltonian applications in order to obtain well converged results. Even when compared to improved approaches, the PSI still demonstrated considerably better performance with up to a factor of 30 reduction in effort. When the polaron-transformed form of this model is considered, we find that a very small time step is required to obtain converged results. We show that this is due to large errors that occur during the first time step. The polaron-transformed Hamiltonian couples all

modes together in a multiplicative fashion which leads to rapid initial evolution of the SPFs, and as a consequence the linearization is only accurate for short times. Motivated by this, we discuss a simple modification that while likely not optimal, considerably improves the convergence of the dynamics obtained using the PSI. This modification makes use of variable but not adaptive time steps with the goal of using smaller time steps to integrate the initial steps where large numbers of SPFs are unoccupied. Our results suggest that an adaptive time step integration scheme would be beneficial for the PSI. We have briefly discussed one such scheme that has previously been used for the MCTDH case and that we find is not generally useful for the multi-layer case.

Finally, we have considered a series of multi-spin-boson models that require considerably larger numbers of SPFs in order to obtain accurate results. We have presented results obtained using ML-MCTDH wavefunctions with up to 100 SPFs for each node and that contain a total of 1.3×10^9 variational parameters. These results demonstrate that the PSI provides a stable approach even for ML-MCTDH wavefunctions that involve very large coefficient tensors. Furthermore, we find that as the number of SPFs increases, the approximations involved in the PSI become valid for longer times. As a consequence, the number of time steps required to accurately integrate the dynamics decreases as the representation of the wavefunction becomes more accurate.

We have identified two areas in which further development of this approach would be beneficial: adaptive time step control and parallelization of the algorithm. We have briefly discussed some efforts we have made towards addressing these issues and have pointed out the potential shortcomings of these approaches. Development in these areas remains an important area for future work. We believe that the results presented in this paper demonstrate that the PSI, even in its current form, is a robust and efficient approach for evolving ML-MCTDH wavefunctions, and that these results will encourage the implementation of such approaches within pre-existing ML-MCTDH packages. To help facilitate such development, the source code for the implementation of the PSI discussed here will be made available upon request.

ACKNOWLEDGMENTS

L.P.L. and D.R.R. were supported by the Chemical Sciences, Geosciences and Biosciences Division of the Office of Basic Energy Sciences, Office of Science, U.S. Department of Energy

DATA AVAILABILITY

The data that support the findings of this study are available from the corresponding author upon reasonable request.

REFERENCES

- ¹U. Manthe, J. Chem. Phys. **142**, 244109 (2015).
- ²H.-D. Meyer and H. Wang, J. Chem. Phys. **148**, 124105 (2018).
- ³H. Wang and H.-D. Meyer, J. Chem. Phys. **149**, 044119 (2018).
- ⁴T. Weike and U. Manthe, J. Chem. Phys. **154**, 194108 (2021).
- ⁵U. Manthe, H.-D. Meyer, and L. S. Cederbaum, J. Chem. Phys. **97**, 3199 (1992).
- ⁶U. Manthe, H.-D. Meyer, and L. S. Cederbaum, J. Chem. Phys. **97**, 9062 (1992).
- ⁷U. Manthe and A. D. Hammerich, Chem. Phys. Lett. **211**, 7 (1993).
- ⁸A. D. Hammerich, U. Manthe, R. Kosloff, H.-D. Meyer, and L. S. Cederbaum, J. Chem. Phys. **101**, 5623 (1994).
- ⁹A. Raab, G. Worth, H.-D. Meyer, and L. S. Cederbaum, J. Chem. Phys. **110**, 936 (1999).
- ¹⁰O. Vendrell, F. Gatti, D. Lauvergnat, and H.-D. Meyer, J. Chem. Phys. **127**, 184302 (2007).
- ¹¹O. Vendrell, F. Gatti, and H.-D. Meyer, J. Chem. Phys. **127**, 184303 (2007).
- ¹²O. Vendrell, M. Brill, F. Gatti, D. Lauvergnat, and H.-D. Meyer, J. Chem. Phys. **130**, 234305 (2009).
- ¹³O. Vendrell, F. Gatti, and H.-D. Meyer, J. Chem. Phys. **131**, 034308 (2009).
- ¹⁴G. A. Worth, H.-D. Meyer, H. Köppel, L. S. Cederbaum, and I. Burghardt, Int. Rev. Phys. Chem. **27**, 569 (2008).
- ¹⁵Q. Meng and H.-D. Meyer, J. Chem. Phys. **138**, 014313 (2013).
- ¹⁶I. R. Craig, M. Thoss, and H. Wang, J. Chem. Phys. **127**, 144503 (2007).
- ¹⁷H. Wang and M. Thoss, J. Phys. Chem. A **111**, 10369 (2007).
- ¹⁸K. I., T. M., and W. H., J. Phys. Chem. C **111**, 11970 (2007).
- ¹⁹I. R. Craig, M. Thoss, and H. Wang, J. Chem. Phys. **135**, 064504 (2011).
- ²⁰R. Borrelli, M. Thoss, H. Wang, and W. Domcke, Mol. Phys. **110**, 751 (2012).
- ²¹E. Y. Wilner, H. Wang, M. Thoss, and E. Rabani, Phys. Rev. B **92**, 195143 (2015).
- ²²J. Schulze, M. F. Shibl, M. J. Al-Marri, and O. Kühn, J. Chem. Phys. **144**, 185101 (2016).
- ²³M. F. Shibl, J. Schulze, M. J. Al-Marri, and O. Kühn, J. Phys. B **50**, 184001 (2017).
- ²⁴D. Mendive-Tapia, E. Mangaud, T. Firmino, A. de la Lande, M. Desouter-Lecomte, H.-D. Meyer, and F. Gatti, J. Phys. Chem. B **122**, 126 (2018).
- ²⁵G. A. Worth, M. H. Beck, A. Jäckle, O. Vendrell, and H.-D. Meyer, “The mctdh package, version 8.2, (2000). h.-d. meyer version 8.3 (2002), version 8.4 (2007). o. vendrell and h.-d. meyer version 8.5 (2013). version 8.5 contains the ml-mctdh algorithm. current versions: 8.4.20 and 8.5.13 (2020). see <http://mctdh.uni-hd.de/> for a description of the heidelberg mctdh package.”
- ²⁶G. Worth, Comput. Phys. Commun. **248**, 107040 (2020).
- ²⁷H. Wang and H.-D. Meyer, J. Phys. Chem. A **125**, 3077 (2021).
- ²⁸C. M. Hinz, S. Bauch, and M. Bonitz, J. Phys. Conf. Ser. **696**, 012009 (2016).
- ²⁹D. Mendive-Tapia and H.-D. Meyer, J. Chem. Phys. **153**, 234114 (2020).
- ³⁰U. Manthe, J. Chem. Phys. **142**, 244109 (2015).
- ³¹L. Lindoy, *New Developments in Open Quantum System Dynamics*, Ph.D. thesis, Magdalen College, University of Oxford (2019).
- ³²F. A. Schröder and A. W. Chin, Phys. Rev. B. **93**, 29 (2016), arXiv:1507.02202.
- ³³D. Bauernfeind and M. Aichhorn, SciPost Phys. **8**, 24 (2020).
- ³⁴B. Kloss, D. R. Reichman, and Y. B. Lev, SciPost Phys. **9**, 70 (2020).
- ³⁵C. Lubich, Appl. Math. Res. Express **2015**, 311 (2014).
- ³⁶B. Kloss, I. Burghardt, and C. Lubich, J. Chem. Phys. **146**, 174107 (2017).
- ³⁷G. Ceruti and C. Lubich, BIT Numer. Math. , 1 (2021).
- ³⁸M. T. Goodrich and R. Tamassia, *Data Structures & Algorithms in Java*, 5th ed. (John Wiley & Sons, 2010) p. 321.
- ³⁹G. Ceruti, C. Lubich, and H. Walach, SIAM J. Numer. Anal. **59**, 289 (2021).
- ⁴⁰B. Kloss, Y. Bar Lev, and D. Reichman, Phys. Rev. B **97**, 024307 (2018).
- ⁴¹S. Paeckel, T. Köhler, A. Swoboda, S. R. Manmana, U. Schollwöck, and C. Hubig, Ann. Phys. (N. Y.) **411**, 167998 (2019).
- ⁴²U. Manthe, Chem. Phys. **515**, 279 (2018).
- ⁴³H. R. Larsson and D. J. Tannor, J. Chem. Phys. **147**, 044103 (2017).
- ⁴⁴M. Yang and S. R. White, Phys. Rev. B **102**, 094315 (2020).
- ⁴⁵G. Ceruti, J. Kusch, and C. Lubich, arXiv preprint arXiv:2104.05247 (2021).
- ⁴⁶A. Garg, J. N. Onuchic, and V. Ambegaokar, J. Chem. Phys. **83**, 4491 (1985).
- ⁴⁷A. J. Leggett, S. Chakravarty, A. T. Dorsey, M. P. A. Fisher, A. Garg, and W. Zwerger, Rev. Mod. Phys. **59**, 1 (1987).
- ⁴⁸A. Nitzan, *Chemical Dynamics in Condensed Phases* (Oxford University Press, 2006).
- ⁴⁹U. Weiss, *Quantum Dissipative Systems*, 4th ed. (World Scientific Publishing Company, 2012).
- ⁵⁰H. Wang, M. Thoss, and W. H. Miller, J. Chem. Phys. **115**, 2979 (2001).
- ⁵¹T. J. Park and J. C. Light, J. Comp. Phys. **85**, 5870 (1986).
- ⁵²R. B. Sidje, ACM Trans. Math. Softw. **24**, 130 (1998).
- ⁵³P. P. Orth, D. Roosen, W. Hofstetter, and K. Le Hur, Phys. Rev. B **82**, 144423 (2010).
- ⁵⁴D. P. S. McCutcheon, A. Nazir, S. Bose, and A. J. Fisher, Phys. Rev. B **81**, 235321 (2010).
- ⁵⁵A. Winter and H. Rieger, Phys. Rev. B **90**, 224401 (2014).
- ⁵⁶G. D. Filippis, A. de Candia, A. S. Mishchenko, L. M. Cangemi, A. Nocera, P. A. Mishchenko, M. Sasseti, R. Fazio, N. Nagaosa, and V. Cataudella, arXiv preprint arXiv:2103.16222 (2021).
- ⁵⁷J. Joffrin and A. Levelut, J. Phys. (Paris) **36**, 811 (1975).
- ⁵⁸K. Kassner and R. Silbey, J. Phys. Condens. Matter **1**, 4599 (1989).
- ⁵⁹F. L. H. Brown and R. J. Silbey, J. Chem. Phys. **108**, 7434 (1998).
- ⁶⁰C. Artiago, F. Balducci, and A. Scardicchio, Phys. Rev. B **103**, 214205 (2021).

Time Evolution of ML-MCTDH Wavefunctions: Supplementary Information

Lachlan P Lindoy,^{1, a)} Benedikt Kloss,¹ and David R Reichman¹

Department of Chemistry, Columbia University, 3000 Broadway, New York, New York 10027, USA

CONTENTS

I. Linearization of the EOMs	2
A. Constant Mean-Field and Linearization	2
B. Linearization and the Singularity-Free EOMs	3
II. Parallel Integration Scheme for the PSI EOMs	5
A. A Parallel Algorithm	5
B. Results	7
III. Alternative Gauge Conditions for the Singularity-Free EOMs	9
IV. Implementation of the PSI: An Efficient Sum-of-Product Operator Representation	11
A. Partitioning of Indices	12
(B): Common SPF operator indices	12
(C): Common SHF operator indices	13
B. Evaluation of Hamiltonian Matrices	13
(A): Standard Terms	13
(B): Common SPF Hamiltonian Terms	14
(C): Common SHF Hamiltonian Terms	15
V. Further Benchmarks: Convergence With Respect To Krylov Subspace Integrator Parameters	16
VI. Further Benchmarks: Wider Tree Structures	17
A. Spin-Boson Model: $\alpha = 0.5$, $\omega_c = 25\Delta$	17
Comparison with Standard ML-MCTDH	17
Convergence with respect to timestep	18
B. Spin-Boson Model: $\alpha = 2.0$, $\omega_c = 25\Delta$	18
C. Polaron-Transformed Spin-Boson Model: $\alpha = 2.0$, $\omega_c = 2.5\Delta$	19
VII. Further Benchmarks: Multi-Spin-Boson Model	21
A. Convergence With Respect to Bath Size	21
B. Polaron-Transformed Multi-Spin-Boson Model	21
References	22

^{a)}Electronic mail: ll3427@columbia.edu

I. LINEARIZATION OF THE EOMS

A. Constant Mean-Field and Linearization

The ML-MCTDH EOMs

$$\dot{\mathbf{A}}^1(t) = -i \left(\frac{1}{\hbar} \mathbf{h}^1(t) - \mathbf{X}^1(t) \right) \mathbf{A}^1(t), \quad (1)$$

and

$$\dot{\mathbf{A}}^{z_l}(t) = -\frac{i}{\hbar} \mathbf{Q}^{z_l}(t) \sum_r \mathbf{h}_r^{z_l}(t) \mathbf{A}^{z_l}(t) \mathbf{H}_r^{z_l}(t) \boldsymbol{\rho}^{z_l}(t)^{-1} - i \mathbf{A}^{z_l}(t) \mathbf{x}^{z_l}(t) + i \mathbf{X}^{z_l}(t) \mathbf{A}^{z_l}(t) \quad (2)$$

are a non-linear set of coupled differential equations that define the evolution of the coefficient tensors at each node of the ML-MCTDH wavefunction. The coupling between these equations arises from the dependence of the Hamiltonian matrices and mean-field density matrices on the coefficient tensors of each node. These equations can be solved directly, using general purpose integration schemes suitable for non-linear ODEs, and such approaches are referred to as variable mean-field (VMF) integration schemes.¹ However, in many situations it is beneficial to use alternative schemes developed specifically for the ML-MCTDH approach. A commonly employed alternative is based on the use of the constant mean-field (CMF) approximation.¹⁻³ To obtain such a scheme, we start by expanding the configurations and SHF coefficient tensors present in the mean-field density matrix and SPF and mean-field Hamiltonian matrices using a Taylor series expansion around a point t to a time $t + dt$. Performing this expansion and using the standard choice of the constraint operator ($\mathbf{x}^{z_l}(t) = \mathbf{0}$) for simplicity, the ML-MCTDH EOMs become

$$\dot{\mathbf{A}}^1(t) = -\frac{i}{\hbar} \mathbf{h}_t^1 \mathbf{A}^1(t) + \mathcal{O}(dt), \quad (3)$$

and

$$\dot{\mathbf{A}}^{z_l}(t) = -\frac{i}{\hbar} \mathbf{Q}^{z_l}(t) \sum_r \mathbf{h}_{rt}^{z_l} \mathbf{A}^{z_l}(t) \mathbf{H}_{rt}^{z_l} (\boldsymbol{\rho}_t^{z_l})^{-1} + \mathcal{O}(dt), \quad (4)$$

where we have introduced the notation \mathbf{O}_t to denote the now time-independent matrix obtained when $\mathbf{O}(t)$ is evaluated using the coefficient tensors obtained at time t . Truncating these equations to lowest order in dt , we obtain the first-order CMF scheme. This corresponds to a forward Euler integration scheme. In practice higher order integration schemes are used.¹⁻³ However, in all CMF approaches the EOMs for each node are independent, and as such it is possible to solve them in parallel. The EOM for the root node is linear in the coefficient tensors and so can be formally solved to give

$$\mathbf{A}^1(t + dt) = \exp \left[-\frac{i}{\hbar} \mathbf{h}_t^1 dt \right] \mathbf{A}^1(t) + \mathcal{O}(dt^2). \quad (5)$$

During each time step the root node coefficient tensor experiences unitary dynamics under the constant Hamiltonian matrix that is obtained by expressing the Hamiltonian operator in terms of an orthonormal, incomplete basis of configurations associated with the root node. These configurations change at each time step but are constant through a step. The EOM for all other nodes are non-linear due to the presence of the projector, and typically general purpose integrators are used for treating these equations. This, however, is not the only possible approach. We can instead further approximate Eq. 4 by inserting a Taylor series expansion of the coefficient tensors $\mathbf{A}^{z_l}(t)$ that are present in the projector $\mathbf{Q}^{z_l}(t)$. Doing this gives rise to linear EOMs for each non-root node which have the same leading error as Eq. 4. As was the case for the CMF integration schemes, it is possible to obtain higher order methods through the use of more sophisticated linearization schemes. These now linear uncoupled EOMs can be formally solved to give

$$\mathbf{A}^{z_l}(t + dt) = \exp \left[-\frac{i}{\hbar} dt \mathbf{Q}_t^{z_l} \mathcal{H}_t^{z_l} \right] \mathbf{A}^{z_l}(t) + \mathcal{O}(dt^2), \quad (6)$$

Here we have introduced the operators $\mathbf{Q}_t^{z_l}$ and $\mathcal{H}_t^{z_l}$, defined by

$$\mathbf{Q}_t^{z_l} \mathbf{A} = \mathbf{Q}_t^{z_l} \mathbf{A}, \quad (7)$$

and

$$\mathcal{H}_t^{z_l} \mathbf{A} = \sum_r \mathbf{h}_{rt}^{z_l} \mathbf{A} \mathbf{H} (\boldsymbol{\rho}_t^{z_l})^{-1}. \quad (8)$$

During each time step the non-root node coefficient tensors experience unitary dynamics under a projected Hamiltonian matrix. This Hamiltonian matrix is obtained by expressing the Hamiltonian operator in terms of a non-orthonormal, incomplete basis that is constructed using a direct product of the configurations and SHFs associated with this node. This will be important in the discussion of alternative equations of motion for evolving ML-MCTDH wavefunctions that are free of singularities.

B. Linearization and the Singularity-Free EOMs

In order to demonstrate that the singularity-free EOMs can be used to evolve the ML-MCTDH wavefunction, we will start by linearizing the ML-MCTDH EOMs for the root node,

$$\dot{\tilde{\mathbf{A}}^1}(t) = \dot{\mathbf{A}}^1(t) = -i \left(\frac{1}{\hbar} \mathbf{h}^1(t) - \mathbf{X}^1(t) \right) \tilde{\mathbf{A}}^1(t), \quad (9)$$

and non-root nodes,

$$\dot{\mathbf{A}}^{z_l}(t) = -\frac{i}{\hbar} \mathbf{Q}^{z_l}(t) \sum_r \mathbf{h}_r^{z_l}(t) \tilde{\mathbf{A}}^{z_l}(t) \tilde{\mathbf{H}}_r^{z_l}(t) (\mathbf{R}^{z_l}(t))^{-1} - i \mathbf{A}^{z_l}(t) \mathbf{x}^{z_l}(t) + i \mathbf{X}^{z_l}(t) \mathbf{A}^{z_l}(t). \quad (10)$$

For the root node, we obtain the same result as in the standard ML-MCTDH representation (Eq. 3), while for the non-root nodes we may write

$$\dot{\mathbf{A}}^{z_l}(t) = -\frac{i}{\hbar} \mathbf{Q}_{t+dt}^{z_l} \sum_r \mathbf{h}_{rt}^{z_l} \mathbf{A}^{z_l}(t) \mathbf{R}_t^{z_l} \tilde{\mathbf{H}}_{rt}^{z_l} (\mathbf{R}_t^{z_l})^{-1} + \mathcal{O}(dt), \quad (11)$$

where we have used the same notation as in Sec. IA, and we have expanded $\mathbf{Q}^{z_l}(t)$ around the point $t + dt$. As was the case for the standard ML-MCTDH EOM, each of these equations are independent of each other. As such, they can each be formally solved to give

$$\mathbf{A}^{z_l}(t + dt) = \exp \left[-\frac{i}{\hbar} dt \mathbf{Q}_{t+dt}^{z_l} \mathcal{H}_{\mathbf{R}^{z_l}t}^{z_l} \right] \mathbf{A}^{z_l}(t) + \mathcal{O}(dt^2), \quad (12)$$

where $\mathbf{Q}_{t+dt}^{z_l}$ is given in Eq. 7, and

$$\mathcal{H}_{\mathbf{R}^{z_l}t}^{z_l} \mathbf{A} = \sum_r \mathbf{h}_{rt}^{z_l} \mathbf{A} \mathbf{R}_t^{z_l} \tilde{\mathbf{H}}_{rt}^{z_l} (\mathbf{R}_t^{z_l})^{-1}. \quad (13)$$

Whenever the mean-field density matrix is singular, Eq. 12 requires the evaluation of the exponential of an unbounded superoperator, and as such, we are not able to evaluate this term without regularisation. If, however, we apply the matrix $\mathbf{R}_t^{z_l} = \mathbf{R}^{z_l}(t)$ to both sides of this equation, we find

$$\mathbf{A}^{z_l}(t + dt) \mathbf{R}^{z_l}(t) = \left(\exp \left[-\frac{i}{\hbar} dt \mathbf{Q}_{t+dt}^{z_l} \mathcal{H}_{\mathbf{R}^{z_l}t}^{z_l} \right] \mathbf{A}^{z_l}(t) \right) \mathbf{R}^{z_l}(t) + \mathcal{O}(dt^2), \quad (14)$$

where the exponentiated superoperator acts only on $\mathbf{A}^{z_l}(t)$. Evaluating the action of the exponential of the superoperator on $\mathbf{A}^{z_l}(t)$, we obtain

$$\mathbf{A}^{z_l}(t + dt) \mathbf{R}^{z_l}(t) = \exp \left[-\frac{i}{\hbar} dt \mathbf{Q}_{t+dt}^{z_l} \mathcal{H}_t^{z_l} \right] \tilde{\mathbf{A}}^{z_l}(t) + \mathcal{O}(dt^2), \quad (15)$$

where we have now introduced a new Hamiltonian superoperator

$$\mathcal{H}_t^{z_l} \mathbf{A} = \sum_r \mathbf{h}_{rt}^{z_l} \mathbf{A} \tilde{\mathbf{H}}_{rt}^{z_l}, \quad (16)$$

and have made no further approximations. Eq. 15 requires the evaluation of the action of the exponential of a bounded superoperator on the transformed coefficient tensor, which no longer requires the use of regularisation. In principle, this exponential could be applied directly. However, in order to arrive at the PSI EOMs,

$$\dot{\tilde{\mathbf{A}}}^{z_l}(t) = -\frac{i}{\hbar} \sum_r \mathbf{h}_r^{z_l}(t) \tilde{\mathbf{A}}^{z_l}(t) \tilde{\mathbf{H}}_r^{z_l}(t), \quad (17)$$

and

$$\dot{\mathbf{R}}^{z_l}(t) = -\frac{i}{\hbar} \sum_r \mathbf{A}^{z_l \dagger}(t) \mathbf{h}_r^{z_l}(t) \mathbf{A}^{z_l}(t) \mathbf{R}^{z_l}(t) \tilde{\mathbf{H}}_r^{z_l}(t), \quad (18)$$

it is necessary to take an alternative approach. Using the definition of the projector $\mathcal{Q}_{t+dt}^{z_l} = 1 - \mathcal{P}_{t+dt}^{z_l}$, we can apply a Lie-Trotter splitting of the exponential giving

$$\mathbf{A}^{z_l}(t+dt) \mathbf{R}^{z_l}(t) = \exp \left[-\frac{i}{\hbar} (-dt) \mathcal{P}_{t+dt}^{z_l} \mathcal{H}_t^{z_l} \right] \exp \left[-\frac{i}{\hbar} dt \mathcal{H}_t^{z_l} \right] \tilde{\mathbf{A}}^{z_l}(t) + \mathcal{O}(dt^2). \quad (19)$$

The term involving evolution under the unprojected Hamiltonian arises as a linearization of Eq. 17, and so it can be accounted for by using Eq. 17 to evolve $\tilde{\mathbf{A}}^{z_l}(t)$ forward in time through a time step dt . We may therefore rewrite this expression as

$$\mathbf{A}^{z_l}(t+dt) \mathbf{R}^{z_l}(t) = \exp \left[-\frac{i}{\hbar} (-dt) \mathcal{P}_{t+dt}^{z_l} \mathcal{H}_t^{z_l} \right] \tilde{\mathbf{A}}^{z_l}(t+dt) + \mathcal{O}(dt^2). \quad (20)$$

The unitary dynamics arising from the projected Hamiltonian leads to evolution of $\mathbf{R}^{z_l}(t+dt)$, according to a linearization of Eq. 18, backwards in time through the time step $-dt$. Here we have not discussed how the $\mathbf{R}^{z_l}(t+dt)$ and $\mathbf{A}^{z_l}(t+dt)$ factors are constructed at the intermediate step, or alternatively how the $\mathbf{A}^{z_l}(t+dt)$ factor is evaluated at the end. There are a number of different approaches for doing so that have the same order of accuracy as the above integration scheme. The PSI approach is one possible integration scheme for integrating the linearized equations, and is discussed in more detail in Paper II.

The process outlined here leads to integration schemes that are accurate to first order. Sometimes this will not provide satisfactory performance, and it may be beneficial to use higher order schemes. Such approaches can be obtained through the use of higher order linearization and higher order splitting techniques, e.g. Stang splitting.⁴⁻⁶

II. PARALLEL INTEGRATION SCHEME FOR THE PSI EOMS

A. A Parallel Algorithm

The projector splitting integrator (PSI)⁴⁻⁸ is an inherently serial algorithm, requiring sequential updates of the coefficient tensors at each node. This is due to the conversion between the orthonormality conditions that is discussed in section II.C of Paper II. When updating the coefficient tensor at node z_l , the PSI algorithm transforms the coefficient tensors associated with all ancestors of node z_l , such that they satisfy the orthonormality conditions given by Eq. 8 in Paper II. In updating a node, the PSI updates the \mathbf{R}^{z_l} matrix before transferring the orthonormality condition to another node. This updating of the \mathbf{R}^{z_l} alters the coefficient tensors associated with the ancestors of node z_l , and as such it is not possible to update multiple nodes in parallel in a simple way.

In order to parallelize the solution of the EOMs, note that it is not necessary to enforce that the total tree structure satisfies the orthonormality conditions given by Eq. 8. Instead, we can construct all of the transformed coefficient tensors, $\tilde{\mathbf{A}}^{z_l}(t)$, associated with all nodes, and the corresponding $\mathbf{R}^{z_l}(t)$ matrices. Now as

$$\tilde{\mathbf{A}}^{z_l} = \mathbf{A}^{z_l} \mathbf{R}^{z_l}, \quad (21)$$

knowledge of these two matrices for each node in the ML-MCTDH wavefunction is, in principle, sufficient to reconstruct the standard ML-MCTDH representation. E.g. we can construct the standard ML-MCTDH coefficient tensors as

$$\mathbf{A}^{z_l} = \tilde{\mathbf{A}}^{z_l} \left(\mathbf{R}^{z_l} \right)^{-1}. \quad (22)$$

We can update the standard coefficient tensors at each node in parallel, and as discussed in Appendix B of Paper I, we can likewise do this using the $\tilde{\mathbf{A}}^{z_l}(t)$ and $\mathbf{R}^{z_l}(t)$ matrices. For the root node we simply need to evaluate

$$\tilde{\mathbf{A}}^1(t+dt) = \exp \left[-\frac{i}{\hbar} \mathbf{h}_t^1 dt \right] \tilde{\mathbf{A}}^1(t) + \mathcal{O}(dt^2), \quad (23)$$

which is obtained as the solution to the linear ODE

$$\dot{\tilde{\mathbf{A}}}^1(t) = -\frac{i}{\hbar} \mathbf{h}_t^1 \tilde{\mathbf{A}}^1(t). \quad (24)$$

For all non-root nodes, z_l , we have

$$\mathbf{A}^{z_l}(t+dt) \mathbf{R}^{z_l}(t) = \exp \left[-\frac{i}{\hbar} (-dt) \mathcal{P}_{t+dt}^{z_l} \mathcal{H}_t^{z_l} \right] \exp \left[-\frac{i}{\hbar} dt \mathcal{H}_t^{z_l} \right] \tilde{\mathbf{A}}^{z_l}(t) + \mathcal{O}(dt^2). \quad (25)$$

Treating each of the propagators independently we have that

$$\mathbf{A}^{z_l}(t+dt) \mathbf{R}^{z_l}(t+dt) = \tilde{\mathbf{A}}^{z_l}(t+dt) = \exp \left[-\frac{i}{\hbar} dt \mathcal{H}_t^{z_l} \right] \tilde{\mathbf{A}}^{z_l}(t) + \mathcal{O}(dt^2), \quad (26)$$

and

$$\mathbf{R}^{z_l}(t) = \exp \left[-\frac{i}{\hbar} (-dt) \mathcal{P}_{t+dt}^{z_l} \mathcal{H}_t^{z_l} \right] \mathbf{R}^{z_l}(t+dt). \quad (27)$$

Within the PSI approach, the standard coefficient tensor \mathbf{A}^{z_l} is updated by first evolving the transformed coefficient tensor forward in time according to the EOM

$$\dot{\tilde{\mathbf{A}}}^{z_l}(t) = -\frac{i}{\hbar} \mathcal{H}_t^{z_l} \tilde{\mathbf{A}}^{z_l}(t), \quad (28)$$

giving the solution found in Eq. 26. Following which we decompose the transformed coefficient tensor to give

$$\tilde{\mathbf{A}}^{z_l}(t+dt) = \mathbf{A}^{z_l}(t+dt) \mathbf{R}^{z_l}(t+dt). \quad (29)$$

This decomposition is not unique and it is possible to insert any arbitrary unitary factor and its inverse between these two terms. In the PSI approach, this arbitrary unitary matrix does not matter as we make use of both factors in this

decomposition. We set our new standard coefficient tensors for node z_l to $\mathbf{A}^{z_l}(t+dt)$, and transfer the $\mathbf{R}^{z_l}(t+dt)$ to other nodes in the tree. To do this, we backwards time evolve $\mathbf{R}^{z_l}(t+dt)$ according to the EOM

$$\dot{\mathbf{R}}^{z_l}(t) = -\frac{i}{\hbar} \mathcal{P}_{t+dt}^{z_l} \mathcal{H}_t^{z_l} \mathbf{R}^{z_l}(t) \quad (30)$$

to obtain $\mathbf{R}^{z_l}(t)$ and transfer this factor to an adjacent node in the tree. This transfer of the $\mathbf{R}^{z_l}(t)$ factor is what leads to the serial nature of the algorithm, and is what needs to be changed to ensure a parallel algorithm. The factor of $\mathbf{R}^{z_l}(t)$ is simply included in the definition of the transformed coefficient tensor of the parent of node z_l (see Eq. 13 and 14 of Paper II). As such, if we retain this factor in the coefficient tensor of the parent of node z_l we no longer need to apply it back up the tree following the evolution of the coefficient tensors at this node. Instead, all we need to do is remove this contribution from the node z_l to obtain the standard coefficient tensor. In principle, this could be done by evolving the transformed coefficient forward in time from $\tilde{\mathbf{A}}^{z_l}(t)$ to $\tilde{\mathbf{A}}^{z_l}(t+dt)$, and evolving $\mathbf{R}^{z_l}(t)$ forward in time to obtain $\mathbf{R}^{z_l}(t+dt)$, from which we can compute the standard coefficient tensor as

$$\mathbf{A}^{z_l}(t+dt) = \tilde{\mathbf{A}}^{z_l}(t+dt) \left(\mathbf{R}^{z_l}(t+dt) \right)^{-1}. \quad (31)$$

Applying this approach at all non-root nodes in parallel results in updated standard coefficient tensors with leading order error $\mathcal{O}(dt^2)$. However, whenever the ML-MCTDH wavefunction is rank deficient the $\mathbf{R}^{z_l}(t+dt)$ matrix is singular, and this operation is ill-defined. As such, care needs to be taken in the construction of the standard coefficient tensors. As in the standard PSI algorithm, we can construct a new set of coefficient tensors that satisfy the orthonormality conditions required for the standard ML-MCTDH EOMs using Eq. 29. However, this decomposition is not unique. If we make use of both factors, this non-uniqueness is not an issue, however, here we are attempting to avoid transferring the $\mathbf{R}^{z_l}(t)$ matrix to other nodes in the tree structure, and so we will not make use of it. As such, when we apply this decomposition we obtain

$$\tilde{\mathbf{A}}^{z_l}(t+dt) = \mathbf{A}^{z_l'}(t+dt) \mathbf{R}^{z_l'}(t+dt), \quad (32)$$

where the new coefficient tensors $\mathbf{A}^{z_l'}(t+dt)$ differ from the time-evolved coefficient tensors we want by an arbitrary unitary matrix

$$\mathbf{A}^{z_l'}(t+dt) = \mathbf{A}^{z_l}(t+dt) \mathbf{U}(t+dt). \quad (33)$$

If we can work out this unitary matrix, we can evaluate the needed time-evolved coefficient tensor as

$$\mathbf{A}^{z_l}(t+dt) = \mathbf{A}^{z_l'}(t+dt) \mathbf{U}(t+dt)^\dagger. \quad (34)$$

Now, using the semi-unitarity of $\mathbf{A}^{z_l}(t+dt)$, we have

$$\mathbf{A}^{z_l \dagger}(t+dt) \mathbf{A}^{z_l'}(t+dt) = \mathbf{U}(t+dt), \quad (35)$$

but we do not know the value of $\mathbf{A}^{z_l}(t+dt)$. If we instead Taylor series expand this term around the point t , we obtain

$$\left[\mathbf{A}^{z_l \dagger}(t) + dt \dot{\mathbf{A}}^{z_l \dagger}(t) + dt^2 \ddot{\mathbf{A}}^{z_l \dagger}(t) + \dots \right] \mathbf{A}^{z_l'}(t+dt) = \mathbf{U}(t+dt). \quad (36)$$

Now, we can further simplify this to find

$$\mathbf{A}^{z_l \dagger}(t) \mathbf{A}^{z_l'}(t+dt) + dt \dot{\mathbf{A}}^{z_l \dagger}(t) \mathbf{A}^{z_l'}(t) \mathbf{U}(t+dt) + \mathcal{O}(dt^2) = \mathbf{U}(t+dt). \quad (37)$$

For the standard PSI gauge this gives

$$\mathbf{U}(t+dt) = \mathbf{A}^{z_l \dagger}(t) \mathbf{A}^{z_l'}(t+dt) + \mathcal{O}(dt^2). \quad (38)$$

For alternative choices of the dynamic gauge conditions there is an additional first order contribution to this expression. In Ref. 9 a parallel version of the PSI integrator for the MCTDH wavefunction is presented that makes use of this representation of the $\mathbf{U}(t+dt)$. In this scheme, the transformed coefficient tensors at each child node are time evolved, the standard coefficient tensors are formed, and the conjugate transpose of this (approximate) unitary factor is absorbed into the root node, following which the root node is evolved. This is not the only possible scheme, and indeed in Ref. 10 an integration scheme for the invariant EOMs is presented that allows for all nodes to be updated

in parallel, and does not require transfer of factors between nodes in the tree structure. This scheme does not apply the matrix $\mathbf{U}(t + dt)$ given by Eq. 38, it instead notes that this matrix is not unitary, and application of this matrix will lead to a reduction in the norm of the wavefunction, and instead uses a modified form of this matrix in which the columns have been normalized. This does not alter the overall order of the approximation but may reduce the errors associated with the reduction in the norm of the matrix. This change does not generally lead to a unitary approximation to $\mathbf{U}(t + dt)$. However, it is possible to construct a unitary approximation that is accurate to the same error ($\mathcal{O}(dt^2)$). To do this we note that the matrix of singular values of the matrix given in Eq. 38 differs from the identity matrix by a term that scales as $\mathcal{O}(dt^2)$, so by performing a singular value decomposition of this matrix and replacing the singular values matrix with the identity matrix, we obtain an approximation to this matrix that is unitary, and has the same $\mathcal{O}(dt^2)$ error as the non-unitary approximations given above. To demonstrate that such a scheme provides a way of integrating the PSI EOMs, we will now consider an application of it to the 500 mode spin-boson model considered in section III.B of Paper II.

B. Results

We have applied the first order parallel integration scheme discussed above to the integration of the PSI EOMs for a 500 mode spin-boson model with $\alpha = 2.0$, $\omega_c = 25\Delta$. We have once again looked at the convergence of the dynamics with respect to time step, and have considered the same tree structure and integration time as was considered in Fig. 4 of Paper II. In Table I, we present the convergence of the dynamics to a reference calculation obtained using the serial PSI with $dt\Delta = 6.25 \times 10^{-4}$. Here we have considered three different first-order integration schemes.

- Parallel: A completely parallel integration scheme that avoids the backward in time propagation of the \mathbf{R}^{z_i} matrices and allows for the coefficient tensors of each node to be evolved in parallel.
- Serial: The first order version of the PSI that only makes use of the forward step and sequentially updates the transformed coefficient tensors.
- No \mathbf{R}^{z_i} evolution: A combination of the two integration schemes that uses the serial updating pattern of the first-order PSI approach, but avoids the backwards in time propagation of the \mathbf{R}^{z_i} matrices by making use of the parallelizable approximation discussed above.

$dt\Delta$	Parallel			Serial		No \mathbf{R}^{z_i} Evolution	
	N_{MF}	ΔP	$\langle N_H \rangle$	ΔP	$\langle N_H \rangle$	ΔP	$\langle N_H \rangle$
4×10^{-2}	25	2.0×10^{-1}	5.8×10^2	8.4×10^{-3}	6.4×10^2	2.2×10^{-2}	6.2×10^2
1×10^{-2}	85	3.9×10^{-2}	1.1×10^3	4.8×10^{-5}	1.1×10^3	2.7×10^{-2}	1.1×10^3
2.5×10^{-3}	325	1.2×10^{-2}	3.0×10^3	5.0×10^{-6}	2.9×10^3	1.6×10^{-3}	3.0×10^3
6.25×10^{-4}	1285	6.2×10^{-3}	9.6×10^3	2.6×10^{-6}	9.3×10^3	2.0×10^{-4}	9.3×10^3
1.5625×10^{-4}	5125	3.5×10^{-4}	3.1×10^4	8.4×10^{-7}	3.1×10^4	1.2×10^{-5}	3.1×10^4
3.90625×10^{-5}	20485	3.3×10^{-5}	1.0×10^5	1.4×10^{-7}	1.1×10^5	7.5×10^{-7}	1.0×10^5
9.765625×10^{-6}	81925	1.7×10^{-6}	4.1×10^5	9.9×10^{-9}	4.1×10^5	8.0×10^{-8}	4.1×10^5

Table I. Convergence of the relative deviations of the population dynamics for a spin-boson model with $N = 500$ bath modes and with $\alpha = 2.0$, $\omega_c = 25\Delta$ obtained using three first-order integration schemes. Here the method labelled parallel is an entirely parallelizable variant of the PSI, the serial method corresponds to the standard serial PSI approach but only uses the forward loop steps, while the “No \mathbf{R}^{z_i} Evolution” method uses the serial updating scheme of the first order PSI but makes use of the parallelizable approximation when evolving the coefficient tensors that avoid the backwards in time propagation of the \mathbf{R}^{z_i} matrices. For both methods, results obtained using the second-order, serial PSI with a time step of $dt\Delta = 6.25 \times 10^{-4}$ were used as the reference calculation.

These results demonstrate that the dynamics obtained using all three of these schemes converge towards the results obtained with the second order PSI, supporting the fact that the parallel integration scheme provides a valid approach for solving the PSI EOMs. However, the convergence of the parallel scheme occurs at a significantly slower rate than was observed for the serial algorithm. Convergence of the deviation to less than 10^{-4} is not obtained until $dt \lesssim 4 \times 10^{-5}$, compared to $dt \lesssim 1 \times 10^{-2}$ that was required using both the first and second order serial schemes. In fact, the parallel integration scheme requires comparable numbers of Hamiltonian applications to the standard ML-MCTDH calculations presented in Ref. 11. If tighter tolerances are required, this approach can outperform standard ML-MCTDH, but it is still less efficient than approaches that make use of improved regularisation schemes,¹¹ and roughly 2 orders of magnitude less efficient than either the serial PSI approach. As a result, this approach is not practical for large scale simulations. The key limitation in the accuracy of the parallel approach appears to arise from

the additional approximations involved in constructing the standard ML-MCTDH representation after the coefficient tensors have been propagated. This is further supported by considering the results obtained using the “No \mathbf{R}^{z_i} evolution” method, that makes use of the serial scheme for updating the coefficient tensors but uses the parallelizable approximation to avoid the backwards in time evolution of the \mathbf{R}^{z_i} matrices. We find once again that this scheme performs considerably worse than the fully serial PSI, although it does show slightly more rapid convergence than the fully parallelizable scheme.

The fully parallelizable scheme we have discussed here is closely related to the approach presented in Ref. 10 for integrating the invariant EOMs. That approach makes use of a higher order scheme for evolving the transformed coefficient tensors at each node, as well as an adaptive time step controller, and so may provide some improvements over the parallel schemes considered here. However, the approach presented in Ref. 10, makes use of a very similar scheme to avoid the backwards in time evolution of the \mathbf{R}^{z_i} matrices, which we find to be the dominant sources of error. Whether similar performance issues are observed for the invariant EOMs approach, or whether the use of an alternative dynamic gauge condition leads to improved accuracy, remains to be seen.

While the scheme we have discussed here is fully parallelizable, it is not a practical method. It exhibits considerably poorer performance than the serial PSI, at least for this problem. This poor performance appears to arise due to the strategy used for constructing the standard ML-MCTDH coefficient tensors from the transformed coefficient tensors. Whether alternative strategies exist that would improve this performance is an open question, and will be left as future work.

III. ALTERNATIVE GAUGE CONDITIONS FOR THE SINGULARITY-FREE EOMS

As in the case of the standard ML-MCTDH approach, it is possible to make use of alternative gauge conditions for the singularity-free EOMS. One choice for standard ML-MCTDH, which provides numerical benefits in some situations, involves partitioning the Hamiltonian into the contributions that are separable and non-separable at each node as

$$\hat{H} = \hat{h}_{sep}^{z_l} + \hat{H}_{sep}^{z_l} + \sum_{r \notin sep} \hat{h}_r^{z_l} \hat{H}_r^{z_l}, \quad (39)$$

$$= \hat{h}_{sep}^{z_l} + \hat{H}_{sep}^{z_l} + \hat{H}_{res}^{z_l}. \quad (40)$$

Here, $\hat{h}_{sep}^{z_l}$ contains all terms in that Hamiltonian that act on the degrees of freedom associated with only one of the children of node z_l , $\hat{H}_{sep}^{z_l}$ contains all terms that only act on the degrees of freedom accounted for by the SHF, and $\hat{H}_{res}^{z_l}$ is the non-separable, residual terms.

Setting the elements of the constraint matrix to^{1,12,13}

$$[\mathbf{x}^{z_l}(t)]_{ij} = \frac{1}{\hbar} \langle \phi_i^{z_l}(t) | \hat{h}_{sep}^{z_l} | \phi_j^{z_l}(t) \rangle \quad (41)$$

leads to an ML-MCTDH EOM for the root node which only depends on the residual part of the Hamiltonian.¹ This can reduce the numerical effort required to solve the ML-MCTDH EOMS whenever the separable contributions to the SPF Hamiltonian are dominant. We can obtain a similar approach for the singularity-free EOMS, if we make use of this constraint matrix for the SPFs and set the elements of the transformed SHF constraint matrix to

$$[\mathbf{y}^{z_l}(t)]_{ij} = \frac{1}{\hbar} \langle \Psi_i^{z_l}(t) | \hat{H}_{sep}^{z_l} | \Psi_j^{z_l}(t) \rangle. \quad (42)$$

Inserting these gauge conditions into the singularity-free EOMS (Eqs. 44 and 45 in Paper I) gives

$$\dot{\hat{\mathbf{A}}}^{z_l}(t) = -\frac{i}{\hbar} \sum_{r \notin sep} \mathbf{h}_r^{z_l}(t) \tilde{\mathbf{A}}^{z_l}(t) \tilde{\mathbf{H}}_r^{z_l}(t), \quad (43)$$

and

$$\dot{\mathbf{R}}^{z_l}(t) = -\frac{i}{\hbar} \sum_{r \notin sep} \mathbf{A}^{z_l \dagger}(t) \mathbf{h}_r^{z_l}(t) \mathbf{A}^{z_l}(t) \mathbf{R}^{z_l}(t) \tilde{\mathbf{H}}_r^{z_l}(t). \quad (44)$$

These equations only involve the non-separable contribution to the Hamiltonian associated with node z_l . If the separable terms evolve on a much more rapid timescale than the non-separable terms, fewer Hamiltonian evaluations may be required to evolve a single coefficient tensor through a step.

Gauge	Alternative			Standard	
$dt\Delta$	N_{MF}	ΔP	$\langle N_H \rangle$	ΔP	$\langle N_H \rangle$
4×10^{-2}	50	6.4×10^{-2}	4.9×10^2	1.6×10^{-2}	9.9×10^2
2×10^{-2}	90	9.9×10^{-3}	7.7×10^2	1.6×10^{-4}	1.4×10^3
1×10^{-2}	170	3.6×10^{-4}	1.3×10^3	1.2×10^{-5}	2.1×10^3
5×10^{-3}	330	2.8×10^{-5}	2.2×10^3	5.0×10^{-6}	3.2×10^3
2.5×10^{-3}	650	6.2×10^{-6}	3.9×10^3	3.4×10^{-6}	5.3×10^3
1.25×10^{-3}	1290	3.3×10^{-6}	7.2×10^3	1.8×10^{-7}	9.3×10^3
6.25×10^{-4}	2570	5.5×10^{-7}	1.3×10^4	Reference	1.7×10^4

Table II. Convergence of the relative deviations of the population dynamics obtained using the second order PSI with both an alternative and the standard choice for the gauge conditions for a spin-boson model with $N = 500$ bath modes and with $\alpha = 2.0$, $\omega_c = 25\Delta$. The population dynamics obtained using the second-order serial PSI with the standard choice of gauge conditions with $dt\Delta = 6.25 \times 10^{-4}$ is used as the reference.

In order to explore this, we now consider using the PSI algorithm to integrate these alternative EOMS for the 500 mode spin-boson model with $\alpha = 2.0$, $\omega_c = 25\Delta$, and with the same tree topology and evolution parameters as were considered in Fig. 4 of Paper II. In Table II we present the convergence of the dynamics towards reference calculations

obtained using the PSI with the standard gauge choice and a time step of $dt\Delta = 6.25 \times 10^{-4}$, and provide the results obtained using the standard gauge (and presented in Table III of Paper II) for reference.

Here we observe that the results obtained using this new gauge converge towards the reference, with a deviation of less than 10^{-4} observed for all $dt\Delta \leq 5 \times 10^{-3}$. This convergence is slower than when using the standard gauge, where deviations of less than 10^{-4} are observed for all $dt\Delta \leq 1 \times 10^{-2}$. For a given timestep the deviation obtained using this new gauge is roughly one order of magnitude larger than with the standard gauge, and this can likely be attributed to the larger leading error term associated when applying the standard linearization strategy (or in this case a second order variant of the strategy). In this process we assume that the SPF and SHF basis functions are constant through the evolution. The alternative dynamic gauge used here introduces explicit rotations of these functions that are present even if the functions would otherwise not evolve, and this evolution is not accounted for accurately. Similar behavior has been observed for the CMF integration schemes applied to standard ML-MCTDH.¹ This may possibly be improved through the use of alternative linearization strategies, however, we will not explore this further here. At a given time step, the number of Hamiltonian applications required to obtain the results is considerably smaller when using this new gauge than compared to the standard PSI gauge. This can be attributed to the differences in the forms of the EOMs. For the standard gauge the EOMs involve contributions from all terms in the Hamiltonian. For the new gauge, only those terms that are not separable at the node z_l enter into the EOMs for node z_l . As such, it is not necessary to include the vast majority of terms that are present in the Hamiltonian, and the resultant integration is considerably easier.

IV. IMPLEMENTATION OF THE PSI: AN EFFICIENT SUM-OF-PRODUCT OPERATOR REPRESENTATION

Fast evaluation of the SPF and mean-field Hamiltonian matrices is incredibly important for an efficient implementation of the PSI. For general Hamiltonians, this is not always possible, and the evaluation of these matrices may prevent efficient implementations. However, there are a number of representations that allow for efficient evaluation of these matrices. In this series of two papers (and in particular in Eqs. 16 and 18 of Paper II) we have made use of the sum-of-product operator representation that is commonly used in the standard ML-MCTDH approach. In this representation we write the Hamiltonian in terms of a sum over N_{prod} operators each of which is expressed as a direct product of operators ($\hat{h}_{\alpha,r}$) that each act on a single physical degree of freedom

$$\hat{H} = \sum_{r=1}^{N_{prod}} \bigotimes_{\alpha=1}^D \hat{h}_{\alpha,r}, \quad (45)$$

where D is the total number of physical degrees of freedom in the problem. At each node z_l , we can make use of this representation to write the Hamiltonian operator as a sum over a set of N_{prod} operators, each of which is expressed as a direct product of operators acting on the physical degrees of SPFs and SHFs of this node

$$\hat{H} = \sum_{r=1}^{N_{prod}} \hat{h}_r^{z_l} \hat{H}_r^{z_l}. \quad (46)$$

Here $\hat{h}_r^{z_l}$ and $\hat{H}_r^{z_l}$ are operators acting on the physical degrees of freedom associated with the SPFs and SHFs of node z_l , respectively. We will refer to these operators as the SPF and SHF Hamiltonian operators. These operators are simply direct products of the operators $\hat{h}_{\alpha,r}$, and can be constructed recursively as

$$\hat{h}_r^{z_l} = \bigotimes_k \hat{h}_r^{(z_l,k)}, \quad (47)$$

where $\hat{h}_r^{(z_l,k)}$ is a SPF Hamiltonian operator associated with the k -th child of node z_l , and

$$\hat{H}_r^{(z_l,k)} = \hat{H}_r^{z_l} \bigotimes_{j \neq k} \hat{h}_r^{(z_l,j)}, \quad (48)$$

For each term in this sum it is possible to obtain the SPF and mean-field Hamiltonian matrices (which correspond to $\hat{h}_r^{z_l}$ and $\hat{H}_r^{z_l}$, respectively) independently using the recursive expressions given in Eqs. 16 and 18 of Paper II (or equivalently Eqs. 49 and 50 below). However this approach is generally not optimal, and there are a number of optimisations that can considerably reduce the numerical effort required to evaluate the Hamiltonian matrices.

If either of the operators $\hat{h}_r^{z_l}$ or $\hat{H}_r^{z_l}$ are the identity operator, then the evaluation of the SPF or mean-field Hamiltonian matrix simplifies considerably. The recursive evaluation of the SPF (Eq. 18 of Paper II),

$$\begin{aligned} h_{r;I^{z_l}J^{z_l}}^{z_l} &= \prod_{k=1}^{d^{z_l}} A_{I^{(z_l,k)}i_k}^{*(z_l,k)} h_{r;I^{(z_l,k)}J^{(z_l,k)}}^{(z_l,k)} A_{J^{(z_l,k)}j_k}^{(z_l,k)} \\ &= \prod_{k=1}^{d^{z_l}} M_{r;i_k j_k}^{(z_l,k)}, \end{aligned} \quad (49)$$

and mean-field Hamiltonian matrices (Eq. 18 of Paper II),

$$\tilde{H}_{r;ab}^{(z_l,k)} = U_{I_{k;a}^{z_l}i}^{*z_l} \left(\prod_{\substack{k'=1 \\ k' \neq k}}^{d^{z_l}} M_{r;i_{k'}j_{k'}}^{(z_l,k')} \right) \tilde{H}_{r;i_j}^{z_l} U_{I_{k;b}^{z_l}j}^{z_l} \quad (50)$$

are simply efficient ways for evaluating the matrix elements of the Hamiltonian operators with respect to the orthonormal set of functions given by the SPFs and transformed SHFs, respectively. As such, if these operators are the identity operator, these matrix elements reduce to the overlap of these functions, and therefore the matrix representation of any identity operators is simply the identity matrix. Thus, we do not need to explicitly evaluate the SPF

and mean-field Hamiltonian matrices that arise from terms where $\hat{h}_r^{z_l} = \hat{1}$ or $\hat{H}_r^{z_l} = \hat{1}$. In many cases, and for the models considered here, this significantly reduces the number of operations that need to be performed.

Another significant improvement occurs if any two (or more) of the operators $\hat{h}_r^{z_l}$ are identical or any two (or more) operators $\hat{H}_r^{z_l}$ are identical, then it is possible to further simplify Eq. 46. In order to do this, we will start by introducing the notation $\hat{h}_{c;i}^{z_l}$ ($\hat{H}_{c;i}^{z_l}$) to denote an operator acting on the SPF (SHF) degrees of freedom that is common to the set of terms with indices $\mathbf{r}_i^{h; z_l}$ ($\mathbf{r}_i^{H; z_l}$) in the sum in Eq. 46. We will suppose that we have $I^{h; z_l}$ and $I^{H; z_l}$ common SPF and SHF operators, respectively. We will also introduce the notation $\mathbf{r}^{ind; z_l}$ to denote the indices of operators that do not contain any of these common operators. Using this notation, we may rewrite Eq. 46 as

$$\hat{H} = \sum_{r \in \mathbf{r}^{ind; z_l}} \hat{h}_r^{z_l} \hat{H}_r^{z_l} + \sum_{i=1}^{I^{h; z_l}} \hat{h}_{c;i}^{z_l} \sum_{r \in \mathbf{r}_i^{h; z_l}} \hat{H}_r^{z_l} + \sum_{i=1}^{I^{H; z_l}} \hat{H}_{c;i}^{z_l} \sum_{r \in \mathbf{r}_i^{H; z_l}} \hat{h}_r^{z_l}. \quad (51)$$

We next introduce the notation

$$\hat{h}_{s;i}^{z_l} = \sum_{r \in \mathbf{r}_i^{H; z_l}} \hat{h}_r^{z_l} \quad \text{and} \quad \hat{H}_{s;i}^{z_l} = \sum_{r \in \mathbf{r}_i^{h; z_l}} \hat{H}_r^{z_l} \quad (52)$$

for the sums of operators that act on the physical degrees of freedom associated with the SPFs and SHFs, respectively. Now Eq. 51 becomes

$$\hat{H} = \underbrace{\sum_{r \in \mathbf{r}^{ind; z_l}} \hat{h}_r^{z_l} \hat{H}_r^{z_l}}_{(A)} + \underbrace{\sum_{i=1}^{I^{h; z_l}} \hat{h}_{c;i}^{z_l} \hat{H}_{s;i}^{z_l}}_{(B)} + \underbrace{\sum_{i=1}^{I^{H; z_l}} \hat{H}_{s;i}^{z_l} \hat{h}_{c;i}^{z_l}}_{(C)}. \quad (53)$$

This expression is still in the form of a sum-of-product operator representation, now with a potentially reduced number of terms in the sum. It is no longer possible to use the recursive expressions for the SPF and mean-field density matrices given by Eqs. 49 and 50. It is necessary to make use of different strategies for evaluating these matrices depending on the terms from which they arise from. In order to make use of this representation it is necessary to evaluate the $I^{h; z_l}$ sets of indices $\mathbf{r}_i^{h; z_l}$, the $I^{H; z_l}$ sets of indices $\mathbf{r}_i^{H; z_l}$, and the remaining set of indices $\mathbf{r}^{ind; z_l}$. We will now present a recursive approach for constructing these sets of indices.

A. Partitioning of Indices

(B): Common SPF operator indices

We start by considering the leaf node of the ML-MCTDH wavefunction tree that corresponds to the physical degree of freedom α , which we will label by l_α . Now we can express the sum-of-product Hamiltonian given by Eq. 45 in the form given by Eq. 46 as

$$\hat{H} = \sum_{r=1}^{N_{prod}} \hat{h}_{\alpha,r} \bigotimes_{\beta \neq \alpha}^D \hat{h}_{\beta,r} = \sum_{r=1}^{N_{prod}} \hat{h}_{\alpha,r} \hat{H}_r^{l_\alpha} = \sum_{r=1}^{N_{prod}} \hat{h}_r^{l_\alpha} \hat{H}_r^{l_\alpha}. \quad (54)$$

The SPF Hamiltonian operators acting on the leaf nodes are the primitive Hamiltonian operators associated with the physical degree of freedom α , and so we can immediately construct the indices $\mathbf{r}_i^{h; z_l}$ for the common SPF Hamiltonian operator terms by inspecting these primitive Hamiltonian operators. For all non-leaf nodes, we need to use the recursive relation for the SPF Hamiltonian operators in order to construct these indices. From the recursive definition of the SPF Hamiltonian operators of a node z_l , the operators $\hat{h}_{c;i}^{z_l}$ must satisfy

$$\hat{h}_{c;i}^{z_l} = \hat{h}_r^{z_l} = \bigotimes_k \hat{h}_r^{(z_l, k)} = \bigotimes_k \hat{h}_{c; i_k}^{z_l, k} \quad \forall r \in \mathbf{r}_i^{h; z_l}. \quad (55)$$

In order for $\hat{h}_{c;i}^{z_l} = \hat{h}_r^{z_l} \quad \forall r \in \mathbf{r}_i^{h; z_l}$, it is necessary that the operators $\hat{h}_r^{z_l, k}$ are also the same for all $r \in \mathbf{r}_i^{h; z_l}$. If we denote the set of indices for which the operator $\hat{h}_r^{(z_l, k)} = \hat{h}_{c; i_k}^{z_l, k}$ as $\mathbf{r}_{i_k}^{h; z_l, k}$, we have that $\mathbf{r}_i^{h; z_l} \subseteq \mathbf{r}_{i_k}^{h; z_l, k} \quad \forall$ children

(z_l, k) of node z_l . Moreover, we can construct the indices $r \in \mathbf{r}_i^{h; z_l}$ as the intersection of these sets $\mathbf{r}_{i_k}^{h; z_l, k}$, that is

$$\mathbf{r}_i^{h; z_l} = \bigcap_k \mathbf{r}_{i_k}^{h; (z_l, k)}, \quad (56)$$

where \bigcap_k denotes the intersection of all the sets indexed by k . In order to obtain all of the sets of indices $\mathbf{r}_i^{h; z_l}$ for all $i = 1, \dots, I^{h; z_l}$, it is necessary to evaluate Eq. 56 for all of the values of $i_k = 1, \dots, I^{h; (z_l, k)}$ for each of the child nodes (z_l, k) . We only label those terms where $\mathbf{r}_i^{h; z_l}$ contains at least 2 indices as common SPF operator terms. We can obtain the sets of indices $\mathbf{r}_i^{h; z_l}$ for all nodes z_l by recursively applying this procedure starting from the leaf nodes, and continuing until we reach the root node.

(C): Common SHF operator indices

Having constructed the sets of indices for the common SPF operators, we are now in a positions where we can construct the sets of indices for the common SHF operators. To do this we start by considering the root node. For this node, the Hamiltonian can be written in the form

$$\hat{H} = \left(\sum_{r=1}^{N_{prod}} \hat{h}_r^0 \right) \times 1 = \left(\sum_{r=1}^{N_{prod}} \hat{h}_r^0 \right) \times H^0. \quad (57)$$

As such, for the root node all terms can be treated as having a common mean-field Hamiltonian. For the root node all terms are of the form (B), and we have

$$\mathbf{r}_1^{H; 0} = \{1, 2, \dots, N_{prod}\}. \quad (58)$$

From the recursive definition of the SHF Hamiltonian operators (Eq. 48), we have

$$\hat{H}_{c; i_k}^{(z_l, k)} = \hat{H}_r^{(z_l, k)} = \hat{H}_r^{z_l} \bigotimes_{j \neq k} \hat{h}_r^{(z_l, j)} \quad \forall r \in \mathbf{r}_{i_k}^{H; (z_l, k)} = \hat{H}_{c; i}^{z_l} \bigotimes_{j \neq k} \hat{h}_{c; i_j}^{(z_l, j)}. \quad (59)$$

In order for $\hat{H}_{c; i_k}^{(z_l, k)} = \hat{H}_r^{(z_l, k)} \quad \forall r \in \mathbf{r}_{i_k}^{H; (z_l, k)}$, it is necessary that the operators $\hat{H}_r^{z_l}$ and $\hat{h}_r^{(z_l, j)} \quad \forall j \neq k$ are also common operators for their respective nodes. As a consequence, for each of the children (z_l, k) of node z_l we find $\mathbf{r}_{i_k}^{H; (z_l, k)} \subseteq \mathbf{r}_i^{H; z_l}$ and $\mathbf{r}_{i_k}^{H; (z_l, k)} \subseteq \mathbf{r}_{i_j}^{h; (z_l, j)} \quad \forall j \neq k$. Moreover, we can construct the indices $r \in \mathbf{r}_i^{H; (z_l, k)}$ as the intersection of the SPF sets $\mathbf{r}_{i_j}^{h; (z_l, j)}$ for the sibling nodes of (z_l, k) and the SHF set $\mathbf{r}_i^{H; z_l}$ of the parent node z_l . That is

$$\mathbf{r}_{i_k}^{H; (z_l, k)} = \mathbf{r}_i^{H; z_l} \bigcap_{j \neq k} \mathbf{r}_{i_j}^{h; (z_l, j)}. \quad (60)$$

Now, as was the case for the common SPF Hamiltonian terms, it is necessary to evaluate these intersections for all allowed values of $i = 1, \dots, I^{H; z_l}$, and $i_j = 1, \dots, I^{h; (z_l, j)}$ in order to construct all of the different $\mathbf{r}_{i_k}^{H; (z_l, k)}$ for $i_k = 1, \dots, I^{H; (z_l, K)}$. This expression can be applied recursively moving down the tree structure, provided the common SPF indices have been evaluated. Once we have constructed all of the sets of indices corresponding to the common SPF and SHF Hamiltonian operators at each node, the remaining set $\mathbf{r}^{ind; z_l}$ is the set of all of the indices that have not already been assigned to a set. Having given recursive expressions that enable us to construct the representation given by Eq. 53 for each node, we will now discuss the process through which the Hamiltonian matrices corresponding to these terms can be evaluated.

B. Evaluation of Hamiltonian Matrices

(A): Standard Terms

The terms in sum (A) in Eq. 53, are exactly of the form given in the naive sum-of-product representation for the Hamiltonian. As such, these terms can be treated in exactly the same manner as the standard terms. In other words

the Hamiltonian matrices can be constructed using Eqs. 49 and 50. The Hamiltonian matrices of other nodes that are used in this expression will not necessarily correspond to terms in the sum (A) for these nodes. In particular, for the evaluation of the SPF Hamiltonian matrices of node z_l , may involve SPF Hamiltonian matrices of node (z_l, k) that are common to multiple indices r . However, as we will see below, the SPF Hamiltonian matrices associated with these common terms are evaluated using Eq. 49. Similar arguments hold for the evaluation of the mean-field Hamiltonian matrices. Importantly, the Hamiltonian matrices for node z_l associated with these terms never depend on the matrices associated with operators $\hat{h}_{s;i}^\alpha$ or $\hat{H}_{s;i}^\alpha$ for any node α .

(B): Common SPF Hamiltonian Terms

The evaluation of the Hamiltonian matrices associated with the terms $\hat{h}_{c;i}^{z_l} \hat{H}_{s;i}^{z_l}$ that are present in sum (B) of Eq. 53, is more involved. These are the terms where the SPF Hamiltonian operator is common to many values of $r \in \mathbf{r}_i^{h; z_l}$, and the SHF Hamiltonian operator is a sum over many different terms. The SPF Hamiltonian terms can be obtained recursively according to Eq. 55. As such, the SPF Hamiltonian matrix corresponding to the term $\hat{h}_{c;i}^{z_l}$ can be obtained using an expression of the form given by Eq. 49, that now involves the matrices $\mathbf{h}_{c, i_k}^{(z_l, k)}$ that are the SPF Hamiltonian matrices associated with the operators $\hat{h}_{c; i_k}^{(z_l, k)}$.

The evaluation of the mean-field Hamiltonian matrix associated with the terms in sum (B) of Eq. 53 is more involved. Now as $\mathbf{r}_i^{h; z_l} \subseteq \mathbf{r}_{i_k}^{h; (z_l, k)}$, the sum in

$$\hat{H}_{i_k, s}^{z_l, k} = \sum_{r \in \mathbf{r}_{i_k}^{h; (z_l, k)}} \hat{H}_r^{(z_l, k)} \quad (61)$$

must contain all indices $r \in \mathbf{r}_i^{h; z_l}$ for all values of i where $\mathbf{r}_i^{h; z_l} \cap \mathbf{r}_{i_k}^{h; (z_l, k)} \neq \emptyset$. Grouping all of these terms together, We may rewrite this sum as

$$\hat{H}_{i_k, s}^{(z_l, k)} = \sum_{j \in \mathbf{J}^{h; z_l}} \sum_{r \in \mathbf{r}_j^{h; z_l}} \hat{H}_r^{(z_l, k)} + \sum_{r \in \mathbf{r}_{\setminus \mathbf{J}^{h; z_l}}^{h; (z_l, k)}} \hat{H}_r^{(z_l, k)}, \quad (62)$$

where we have introduced the set

$$\mathbf{J}^{h; z_l} = \{j | \mathbf{r}_j^{h; z_l} \cap \mathbf{r}_{i_k}^{h; (z_l, k)} \neq \emptyset\}, \quad (63)$$

and

$$\mathbf{r}_{\setminus \mathbf{J}^{h; z_l}}^{h; (z_l, k)} = \mathbf{r}_{i_k}^{h; (z_l, k)} \setminus \left(\bigcup_{j \in \mathbf{J}^{h; z_l}} \mathbf{r}_j^{h; z_l} \right). \quad (64)$$

Inserting the recursive definition of the SHF Hamiltonian operators (Eq. 48), this becomes

$$\hat{H}_{i_k, s}^{(z_l, k)} = \sum_{j \in \mathbf{J}^{h; z_l}} \hat{H}_{s, j}^{z_l} \otimes_{l \neq k} \hat{h}_{c, j}^{(z_l, l)} + \sum_{r \in \mathbf{r}_{\setminus \mathbf{J}^{h; z_l}}^{h; (z_l, k)}} \hat{H}_r^{(z_l, k)} \otimes_{j \neq k} \hat{h}_r^{(z_l, j)}. \quad (65)$$

From the above it is clear that we do not need the individual terms that define the operators $\hat{H}_{s, j}^{z_l}$, we only need the overall operator. The mean-field Hamiltonian matrix for the operator $\hat{H}_{i_k, s}^{(z_l, k)}$ can therefore be evaluated as

$$\hat{H}_{i_k, s}^{z_l, k} = \sum_{j \in \mathbf{J}^{h; z_l}} \hat{H}_{s, j}^{z_l} \otimes_{l \neq k} \hat{h}_{c, j}^{z_l, l} + \sum_{r \in \mathbf{r}_{\setminus \mathbf{J}^{h; z_l}}^{h; z_l, k}} \hat{H}_r^{z_l, k} \otimes_{j \neq k} \hat{h}_r^{z_l, j}. \quad (66)$$

In order to evaluate the matrix representation of this operator, it is necessary to construct matrix elements with respect to the transformed SHFs. Doing so for each term we find that the matrix representation of this operator may be expressed as

$$\mathbf{H}_{i_k, s}^{z_l, k} = \sum_{j \in \mathbf{J}^{h; z_l}} \mathbf{M}_{s, j}^{z_l} + \sum_{r \in \mathbf{r}_{\setminus \mathbf{J}^{h; z_l}}^{h; z_l, k}} \mathbf{M}_r^{z_l, k}, \quad (67)$$

where each of the matrices $\mathbf{M}_{s, j}^{z_l}$ and $\mathbf{M}_r^{z_l, k}$ can be calculated according to an equation with the same form as Eq. 50 but using the matrix representations of the operators present in Eq. 66.

(C): Common SHF Hamiltonian Terms

The evaluation of the Hamiltonian matrices associated with the terms $\hat{h}_{s;i}^{z_l} \hat{H}_{c;i}^{z_l}$ that are present in sum (C) of Eq. 53 also requires an alternative approach. As for the type (B) terms, the matrix representation of the common operator in this term ($\hat{H}_{c;i}^{z_l}$) can be evaluated in the standard way. That is, the mean-field Hamiltonian matrix corresponding to $H_{c;i}^{z_l}$ can be obtained using a recursive expression of the form given by Eq. 50, however now involving the matrix representations of the operators present in Eq. 59.

As was the case for the type (B) terms, evaluation of the other term is more involved. The SPF Hamiltonian operator is obtained as a sum over many terms

$$\hat{h}_{s;i}^{z_l} = \sum_{r \in \mathbf{r}_i^{H; z_l}} \hat{h}_r^{z_l}. \quad (68)$$

Now, as $\mathbf{r}_{i_k}^{H; (z_l, k)} \subseteq \mathbf{r}_{i_j}^{H; z_l} \forall k$, we may rewrite the sum over r to give

$$\hat{h}_{s;i}^{z_l} = \sum_k \sum_{j \in \mathbf{J}^{H; (z_l, k)}} \sum_{r \in \mathbf{r}_j^{H; (z_l, k)}} \hat{h}_r^{z_l} + \sum_{r \in \mathbf{r}_{\setminus \mathbf{J}^{H; z_l}}^{H; z_l}} \hat{h}_r^{z_l}, \quad (69)$$

where the sum of k runs over all children of this node, and we have introduced the sets associated with each of the children

$$\mathbf{J}^{H; (z_l, k)} = \{j | \mathbf{r}_i^{H; z_l} \cap \mathbf{r}_j^{H; (z_l, k)} \neq \emptyset\}, \quad (70)$$

and the remaining set of r indices

$$\mathbf{r}_{\setminus \mathbf{J}^{H; z_l}}^{H; z_l} = \mathbf{r}_i^{H; z_l} \setminus \left(\bigcup_k \bigcup_{j \in \mathbf{J}^{H; (z_l, k)}} \mathbf{r}_j^{H; (z_l, k)} \right). \quad (71)$$

Inserting the recursive definition of the SPF Hamiltonian operator (Eq. 47) gives

$$\hat{h}_{s;i}^{z_l} = \sum_k \sum_{j \in \mathbf{J}^{H; (z_l, k)}} \sum_{r \in \mathbf{r}_j^{H; (z_l, k)}} \bigotimes_{k'} \hat{h}_r^{(z_l, k')} + \sum_{r \in \mathbf{r}_{\setminus \mathbf{J}^{H; z_l}}^{H; z_l}} \bigotimes_{k'} \hat{h}_r^{(z_l, k')}. \quad (72)$$

For each value of $j \in \mathbf{J}^{H; (z_l, k)}$, there is an index $i_{jk'}$ associated with each of the sibling nodes to node (z_l, k) , namely the nodes (z_l, k') for which $\mathbf{r}_j^{H; (z_l, k)} \subset \mathbf{r}_{i_{jk'}}^{H; (z_l, k')}$. All of the r indices present in this term are accounted for by common SPF Hamiltonian operator terms in the sibling nodes. As such, we may rewrite the above expression in the form

$$\hat{h}_{s;i}^{z_l} = \sum_k \sum_{j \in \mathbf{J}^{H; (z_l, k)}} \hat{h}_{s;j}^{(z_l, k)} \bigotimes_{k' \neq k} \hat{h}_{c; i_{jk'}}^{(z_l, k')} + \sum_{r \in \mathbf{r}_{\setminus \mathbf{J}^{H; z_l}}^{H; z_l}} \bigotimes_{k'} \hat{h}_r^{(z_l, k')}. \quad (73)$$

The SPF Hamiltonian operator of node z_l can therefore be expressed in terms of direct products between common and sum terms, or general terms. For each term it is possible to construct the matrix representation using a recursive expression of the form given in Eq. 49, and the overall matrix representation of the operator $\hat{h}_{s;i}^{z_l}$ is simply the sum over all of these terms.

This strategy for treating the Hamiltonian can provide considerable performance improvements over the naive sum-of-product representation given in Eq. 46, depending on the form of the Hamiltonian. As an example, for the standard spin-boson model Hamiltonian for a system with N bath modes, the full sum-of-product representation given in Eq. 45 contains $N_{prod} = 2N + 1$ terms. Using this representation it would be necessary to evaluate $\mathcal{O}(N)$ terms in order to construct the Hamiltonian at each node. As the number of nodes scales as $\mathcal{O}(N \log(N))$, the overall algorithm would scale as $\mathcal{O}(N^2 \log(N))$. When using a separation of the system and bath degrees of freedom within the tree structure, this alternative representation requires the evaluation of 3 distinct terms for each node where the SPFs represent solely bath degrees of freedom, and 2 for the other nodes. Using this alternative representation we take the scaling of the approach to $\mathcal{O}(N \log(N))$. For the 10^6 mode problems considered in Paper II that required roughly 30 hours in order to obtain converged results, the use of the naive representation would take $\mathcal{O}(N = 10^6)$ times longer, which would clearly be impractical. Source code capable of constructing the partitioning of the Hamiltonian terms and evaluating the resultant terms will be made available upon request.

V. FURTHER BENCHMARKS: CONVERGENCE WITH RESPECT TO KRYLOV SUBSPACE INTEGRATOR PARAMETERS

In applying the PSI it is necessary to solve the linear ODEs for the transformed coefficient tensors and \mathbf{R}^{z_l} matrices. Here we have done this using an adaptive order, adaptive time step Krylov subspace integration scheme that makes use of the error estimates presented in Ref. 14. In all calculations discussed in the main text we have used a fixed value for the Krylov subspace integrator tolerance, ϵ_{kry} , of $\epsilon_{kry} = 10^{-12}$. Here we now consider the effect this tolerance parameter has on the convergence and efficiency of the PSI calculations. We once again consider the 500 mode spin-boson model with $\alpha = 2.0$, $\omega_c = 25\Delta$ and use the same tree topology and evolution parameters as were considered in Fig. 4 of Paper II. The convergence of the dynamics with respect to time step for various choices of ϵ_{kry} is given in Table III.

ϵ_{kry}	10^{-4}			10^{-6}			10^{-8}		
$dt\Delta$	N_{MF}	ΔP	$\langle N_H \rangle$	ΔP	$\langle N_H \rangle$	ΔP	$\langle N_H \rangle$	ΔP	$\langle N_H \rangle$
4×10^{-2}	50	1.2×10^{-2}	1.3×10^3	1.5×10^{-2}	1.3×10^2	1.5×10^{-2}	9.9×10^2		
2×10^{-2}	90	1.1×10^{-3}	5.2×10^3	1.7×10^{-4}	1.7×10^3	6.7×10^{-5}	1.2×10^3		
1×10^{-2}	170	6.8×10^{-3}	2.1×10^3	2.0×10^{-5}	1.4×10^3	1.8×10^{-5}	1.6×10^3		
5×10^{-3}	330	4.4×10^{-3}	1.6×10^3	1.4×10^{-4}	2.0×10^3	4.4×10^{-6}	2.4×10^3		
2.5×10^{-3}	650	3.5×10^{-2}	2.6×10^3	1.8×10^{-5}	3.4×10^3	3.3×10^{-6}	4.0×10^3		
1.25×10^{-3}	1290	5.4×10^{-3}	5.1×10^3	6.1×10^{-5}	6.3×10^3	1.8×10^{-6}	7.3×10^3		
6.25×10^{-4}	2570	4.1×10^{-4}	1.0×10^4	1.4×10^{-4}	1.1×10^4	8.0×10^{-8}	1.3×10^4		

ϵ_{kry}	10^{-10}			10^{-12}		
$dt\Delta$	N_{MF}	ΔP	$\langle N_H \rangle$	ΔP	$\langle N_H \rangle$	
4×10^{-2}	50	1.3×10^{-2}	8.8×10^2	1.6×10^{-2}	9.9×10^2	
2×10^{-2}	90	1.2×10^{-4}	1.3×10^3	1.6×10^{-4}	1.4×10^3	
1×10^{-2}	170	1.7×10^{-5}	1.8×10^3	1.2×10^{-5}	2.1×10^3	
5×10^{-3}	330	4.2×10^{-6}	2.8×10^3	5.0×10^{-6}	3.2×10^3	
2.5×10^{-3}	650	3.1×10^{-6}	4.6×10^3	3.4×10^{-6}	5.3×10^3	
1.25×10^{-3}	1290	1.7×10^{-6}	8.1×10^3	1.8×10^{-7}	9.3×10^3	
6.25×10^{-4}	2570	1.1×10^{-7}	1.5×10^4	Reference	1.7×10^4	

Table III. The convergence with respect to time step (dt) of the deviation in the population dynamics of a spin-boson model obtained using the projector splitting integrator for various values of the Krylov subspace integration tolerance, ϵ_{kry} . The spin-boson model considered has $\varepsilon/\Delta = 0$, $\alpha = 2.0$, $\omega_c = 25\Delta$, and with $N = 500$ bath modes. These calculations were performed using the same tree topology as was used in the main text and deviations from the reference calculation (indicated in the table) were calculated using dynamics obtained up to $t\Delta = 0.8$.

For $\epsilon_{kry} \geq 10^{-6}$ we observe rather large deviations even at very small time steps. The results obtained are not converged to within a tolerance of 10^{-4} for any of the time steps considered. However, upon decreasing ϵ_{kry} to $\leq 10^{-8}$, we find that the deviations obtained become roughly independent of the value ϵ_{kry} for a given time step, and so a Krylov subspace tolerance of $\epsilon_{kry} \leq 10^{-8}$ is sufficient to converge the dynamics of this model. For all values of $\epsilon_{kry} \leq 10^{-8}$, we find that, unsurprisingly, as the Krylov subspace tolerance increases the number of Hamiltonian applications required decreases. Using a Krylov subspace tolerance of $\epsilon_{kry} \leq 10^{-8}$ leads to a $\sim 25\%$ decrease in the number of Hamiltonian applications required compared to the calculations obtained with $\epsilon_{kry} \leq 10^{-12}$ that are reported in the main text, without significant changes in the accuracy of the calculations. For larger values of the Krylov subspace integration tolerance the inaccurate evolution of the coefficient tensors leads to significantly larger deviations.

VI. FURTHER BENCHMARKS: WIDER TREE STRUCTURES

In addition to the models considered in the main text, we now consider a series of three spin-boson models that have previously been treated using standard ML-MCTDH with improved regularisation schemes.^{11,15} Here we will consider similar tree structures to those considered in Refs. 11 and 15. These correspond to considerably wider tree structures (larger numbers of groups of SPFs at each node) than were considered in the main text.

A. Spin-Boson Model: $\alpha = 0.5$, $\omega_c = 25\Delta$

We first consider a spin-boson model with parameters $\varepsilon/\Delta = 0, \alpha = 0.5, \omega_c = 25\Delta$ and with either $N = 250$ or 1000 bath modes. Following Ref. 11, a three layer ML-MCTDH ansatz is used for $N = 250$, and a four layer tree is used for $N = 1000$. In each case, the top node has six children (five for the bath and one for the system) with each node accounting for bath degrees of freedom using 8 SPFs and 2 SPFs are used for the system node. For all layers below this, each node has up to 4 children and uses 5 SPFs. In all calculations a Krylov subspace integrator tolerance of $\epsilon_{kry} = 10^{-12}$ was used.

Comparison with Standard ML-MCTDH

In Fig. 1, the time-dependent population difference value $P(t) = \langle \hat{\sigma}_z(t) \rangle$ obtained for these two models using the PSI with a time step of $dt\Delta = 0.000625$ are compared to the standard ML-MCTDH results that have previously been reported in Ref. 11.

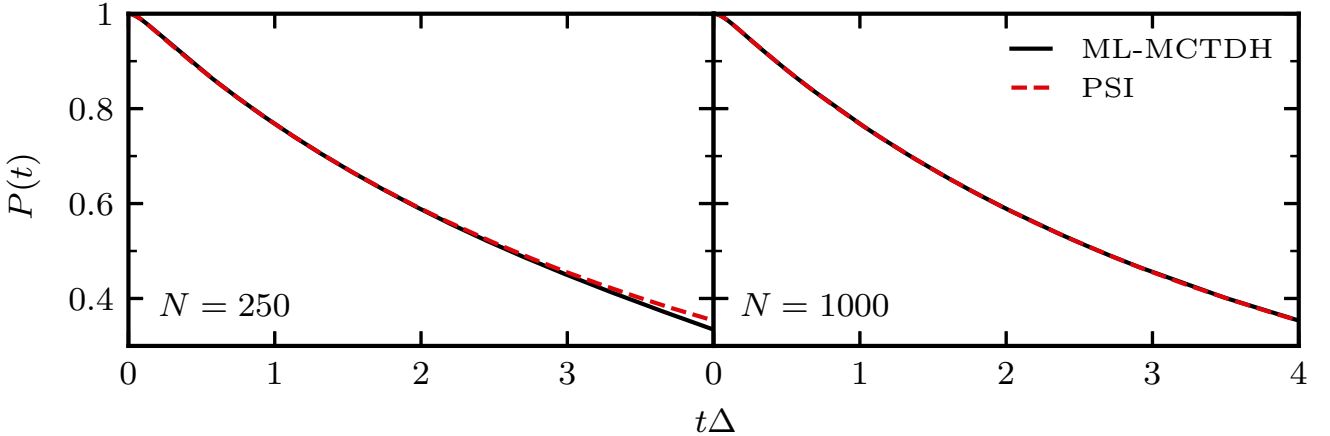


Figure 1. The time-dependent expectation value $P(t)$ obtained for two spin-boson model with $\varepsilon/\Delta = 0$, $\alpha = 0.5$, $\omega_c = 25\Delta$, and with $N = 250$ (left) or $N = 1000$ (right) bath modes. Here the results obtained using the PSI are compared against the results presented in Ref. 11 that were obtained using the standard ML-MCTDH approach.

For $N = 250$, the population dynamics obtained using the PSI agree with the standard ML-MCTDH results for times $t\Delta < 2$. Past this point deviations are observed, with the PSI predicting a larger value of $P(t)$ at longer times. Upon increasing the number of bath modes to $N = 1000$, both approaches agree over the entire period considered ($t\Delta = 4$). In Fig. 2, we compare the results obtained with $N = 250$ and $N = 1000$ that were obtained using the PSI. We see that the two PSI results agree closely over the entire time period considered here (to within the thickness of the lines). As we have attempted to use the same bath discretisation strategy as was used in Ref. 11, it is unclear what leads to this difference in the convergence of dynamics with respect to the number of bath modes for these two approaches.

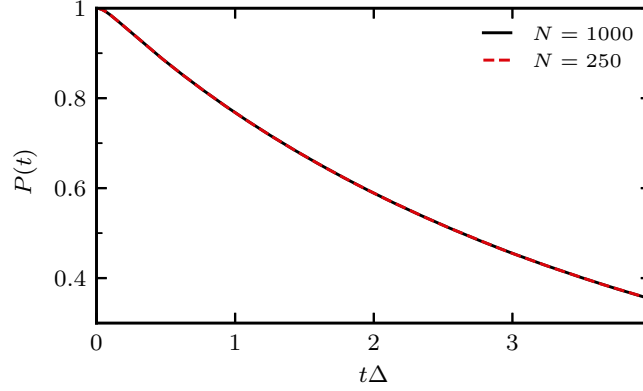


Figure 2. Comparison of the time-dependent expectation value $P(t)$ obtained using the PSI for a spin-boson model with $\varepsilon/\Delta = 0$, $\alpha = 0.5$, $\omega_c = 25\Delta$, and with $N = 250$ and $N = 1000$ bath modes.

Convergence with respect to timestep

In Table IV, we show the convergence of the deviation with respect to the timestep used in the projector splitting integrator. For both bath sizes, a deviation of less than 1×10^{-4} is obtained for all timesteps less than $dt\Delta = 0.02$. For the $N = 250$ case, this corresponds to 410 Hamiltonian evaluations and ~ 4800 Hamiltonian applications in order to obtain dynamics up to $t\Delta = 4$. This corresponds to a factor of ~ 30 and ~ 3 times fewer evaluations and applications, respectively, than were used in previous ML-MCTDH calculations using both standard and improved regularisation strategies (see Table I of Ref. 11). For the $N = 1000$ case, this corresponds to 810 Hamiltonian evaluations and $\sim 10,000$ Hamiltonian applications in order to obtain dynamics up to $t\Delta = 8$. This again corresponds to a factor of ~ 30 and ~ 3 times fewer evaluations and applications, respectively, than were required by previous ML-MCTDH calculations (see Table II of Ref. 11).

N	250			1000		
	N_{MF}	ΔP	$\langle N_H \rangle$	N_{MF}	ΔP	$\langle N_H \rangle$
0.04	210	1.7×10^{-4}	3.4×10^3	410	5.0×10^{-4}	8.9×10^3
0.02	410	1.3×10^{-5}	4.8×10^3	810	3.2×10^{-5}	1.0×10^4
0.01	810	2.2×10^{-6}	7.4×10^3	1610	1.5×10^{-6}	1.5×10^4
0.005	1610	1.2×10^{-6}	1.2×10^4	3210	4.4×10^{-7}	2.4×10^4
0.0025	3210	2.1×10^{-7}	2.2×10^4	6410	2.0×10^{-7}	4.1×10^4
0.00125	6410	2.3×10^{-8}	3.9×10^4	12810	1.9×10^{-8}	7.5×10^4
0.000625	12810	Reference	7.1×10^4	25610	Reference	1.4×10^5

Table IV. The convergence with respect to time step (dt) of the deviation in the population dynamics of a spin-boson model obtained using the projector splitting integrator. The spin-boson model considered has $\varepsilon/\Delta = 0$, $\alpha = 0.5$, $\omega_c = 25\Delta$, and with varying numbers of bath modes, $N = 250$ or 1000. For $N = 250$ and 1000, three and four level tree tensor networks were used, respectively. To allow for a more direct comparison with previously ML-MCTDH calculations¹¹, the deviations obtained for $N = 250$ and 1000 are evaluated to times $t\Delta = 4$ and $t\Delta = 8$, respectively.

As was found for the results shown in Table III of Paper II, there is no significant increase in the deviations obtained for a given time step when increasing the size of the bath. Similarly the number of Hamiltonian evaluations and applications (after dividing by a factor of 2 to account for the longer evolution time in the $N = 1000$ case), does not significantly change when the number of bath modes is increased.

B. Spin-Boson Model: $\alpha = 2.0$, $\omega_c = 25\Delta$

We next reconsider the spin-boson model considered in Paper II, however, with the wider tree structures considered in Refs. 11 and 15. Here we once again consider this model with varying numbers of bath modes ($N = 500, 2000, 5000$, and 10^4). Following Ref. 11, four, five, and six layer ML-MCTDH wavefunctions were used for $N = 500, 2000$, and 5000, respectively, with the root node having five children and each bath node using 8 SPFs. For the $N = 10^4$

N	500		2,000		5,000		10,000	
$dt\Delta$	ΔP	$\langle N_H \rangle$	ΔP	$\langle N_H \rangle$	ΔP	$\langle N_H \rangle$	ΔP	$\langle N_H \rangle$
4×10^{-2}	1.7×10^{-2}	1.2×10^3	8.8×10^{-3}	1.1×10^2	1.1×10^{-2}	1.1×10^2	1.4×10^{-2}	1.5×10^2
2×10^{-2}	2.2×10^{-4}	1.4×10^3	3.6×10^{-4}	1.3×10^3	2.5×10^{-4}	1.5×10^3	5.9×10^{-4}	1.7×10^3
1×10^{-2}	7.1×10^{-5}	2.0×10^3	5.3×10^{-5}	2.0×10^3	7.0×10^{-5}	2.0×10^3	7.7×10^{-5}	2.2×10^3
5×10^{-3}	1.8×10^{-5}	3.1×10^3	1.3×10^{-5}	3.1×10^3	2.0×10^{-6}	3.1×10^3	1.4×10^{-5}	3.3×10^3
2.5×10^{-3}	3.2×10^{-6}	5.0×10^3	1.1×10^{-5}	5.0×10^3	9.5×10^{-6}	5.0×10^3	4.7×10^{-6}	5.1×10^3
1.25×10^{-3}	5.0×10^{-7}	8.8×10^3	4.3×10^{-7}	8.8×10^3	9.1×10^{-7}	8.8×10^3	1.1×10^{-6}	8.8×10^3
6.25×10^{-4}	Reference	1.6×10^4	Reference	1.6×10^4	Reference	1.6×10^4	Reference	1.6×10^4

Table V. The convergence with respect to time step (dt) of the deviation in the population dynamics of a spin-boson model obtained using the projector splitting integrator. The spin-boson model considered has $\varepsilon/\Delta = 0$, $\alpha = 2$, $\omega_c = 25\Delta$, and with varying numbers of bath modes (specified in the tables). The deviations were evaluated using reference calculations obtained with $dt\Delta = 6.25 \times 10^{-4}$ and were computed from dynamics up to $t\Delta = 0.8$.

case, a seven layer ML-MCTDH wavefunction was used with the root node having six children each of which have 8 SPFs, as was considered in Ref. 15. All other nodes had up to 4 children and used 5 SPFs. These correspond to considerably wider but less deeply nested tree structures than were considered in the main text.

In Table V, we show the convergence with respect to time-step of the deviations in the population dynamics obtained for this spin-boson model with varying numbers of bath modes. As was the case for the tree structures considered in the main text, the population dynamics is converged to within a deviation of 10^{-4} for all simulations using a time step of $dt\Delta \leq 0.01$ regardless of the number of bath modes. Furthermore, the convergence behavior does not change significantly compared to the tree topology considered in the main text.

The number of Hamiltonian applications required is essentially independent to the number of bath modes, which supports the conclusion made in the main text that it is the physics of the problem that limits the time step that can be used with the PSI approach.

C. Polaron-Transformed Spin-Boson Model: $\alpha = 2.0$, $\omega_c = 2.5\Delta$

We now consider the final model considered in Ref. 11, a polaron-transformed spin-boson model with $\alpha = 2.0$, $\omega_c = 2.5\Delta$. This spin-boson model corresponds to the 1 TLS case of the multi-spin-boson model that was considered in Paper II. It has previously been found that the standard ML-MCTDH approach can fail to provide converged results¹¹ for this model. It is necessary to use a very small regularisation parameter when treating this polaron-transformed spin-boson model,^{11,16} which leads to very stiff EOMs that can become infeasible to solve. In Ref. 11 converged results were obtained for this model by using an alternative regularisation scheme for the ML-MCTDH EOMs.

$dt\Delta$	Standard			Polaron	
	N_{MF}	ΔP	$\langle N_H \rangle$	ΔP	$\langle N_H \rangle$
3.2×10^{-1}	60	2.0×10^{-4}	9.5×10^2	2.0×10^{-3}	1.2×10^3
1.6×10^{-1}	110	4.9×10^{-5}	1.3×10^3	3.2×10^{-4}	1.4×10^3
8×10^{-2}	210	1.4×10^{-5}	1.9×10^3	5.0×10^{-5}	2.1×10^3
4×10^{-2}	410	3.4×10^{-6}	3.1×10^3	4.0×10^{-6}	3.4×10^3
2×10^{-2}	810	8.2×10^{-7}	5.6×10^3	1.2×10^{-6}	5.8×10^3
1×10^{-2}	1610	1.6×10^{-7}	1.0×10^4	2.9×10^{-7}	1.0×10^4
5×10^{-3}	3210	Reference	1.9×10^4	Reference	1.9×10^4

Table VI. The convergence with respect to time step (dt) of the deviation in the population dynamics of a spin-boson model obtained using the projector splitting integrator. Here we consider convergence of the dynamics obtained using the standard and the polaron-transformed Hamiltonian for a spin-boson model with $\varepsilon/\Delta = 0$, $\alpha = 2$, $\omega_c = 2.5\Delta$, and with $N = 512$ bath modes. In all cases, the dynamics was obtained using the alternative integration scheme described above and the deviation was evaluated for dynamics obtained to times $t\Delta = 8$.

Following Ref. 11, we consider this model with $N = 512$ bath modes. We have used a four layer ML-MCTDH wavefunction, where the root node had six children (five for the bath and one for the system) and each bath node used 8 SPFs while the system node used 2 SPFs. For all other (non-leaf) layers, each node had up to 4 children and used 5 SPFs. In Table VI, we present the the standard and polaron-transformed dynamics obtained using the PSI for this model.

We find that for large time steps slightly fewer function evaluations are required when using the standard spin-boson Hamiltonian compared to the polaron-transformed Hamiltonian and smaller deviations are found. However, upon decreasing the time step the number of Hamiltonian evaluations and the deviations observed from their references become similar. For the standard representation, the dynamics obtained is converged to within a deviation of 10^{-4} by a time step of $dt\Delta = 0.16$, which corresponds to 110 Hamiltonian evaluations and an average of ~ 1300 Hamiltonian evaluations per node. For the polaron-transformed Hamiltonian, convergence is obtained for all time steps less than or equal to $dt\Delta = 0.08$, which required 210 Hamiltonian evaluations and an average of ~ 2100 Hamiltonian evaluations per node. While this problem has previously been treated using standard ML-MCTDH based approaches with improved regularisation schemes, it is difficult to provide a direct comparison between the two sets of results as the timescale over which dynamics has been obtained has not been presented in Ref. 11. Here we have considered the population dynamics up to times $t\Delta = 8$.

By comparing the results for this model to those obtained with $\omega_c = 25\Delta$ (Table V), we see that comparable numerical effort, as measured via the number of Hamiltonian evaluations and applications, is required to obtain a results with comparable accuracy up to $t\Delta = 8$ for this model as is required to obtain results to $t\Delta = 0.8$ for the previous model. This supports the conclusion that the numerical effort associated with the PSI is strongly tied to the physics of the problem. When we reduce the time scale of evolution of the bath by a factor of 10, we are able to increase the time step by a factor of 10 and obtain comparable accuracy.

VII. FURTHER BENCHMARKS: MULTI-SPIN-BOSON MODEL

Finally we will reconsider the multi-spin-boson model that was considered in Sec. III.C of Paper II. We will use the same set of multi-spin-boson model parameters (given in Table IV in Paper II), and only examine the cases where $M = 1$ or 2.

A. Convergence With Respect to Bath Size

We will first investigate the convergence of the population dynamics with respect to the number of frequencies that have been used to discretize the bath. For all calculations in the main text we used $N_b = 512$ modes. Here we will look at considerably larger numbers of bath modes. In all calculations we use the same strategy for constructing the ML-MCTDH wavefunction as discussed in the main text for this model, and will use $N_{spf} = 24$ and 48 for the $M = 1$ and 2 calculations, respectively. For both cases this is sufficient to obtain deviations of less than 10^{-4} (see Table V of Paper II). We present the deviation as a function of the bath size in Table VII. For $M = 1$ convergence

M	1		2	
N	$\langle \Delta P \rangle$	$\langle N_H \rangle$	$\langle \Delta P \rangle$	$\langle N_H \rangle$
128	1.3×10^{-3}	2.7×10^3	1.2×10^{-2}	2.6×10^3
256	6.0×10^{-4}	2.6×10^3	5.2×10^{-3}	2.5×10^3
512	2.6×10^{-4}	2.6×10^3	1.8×10^{-3}	2.5×10^3
1024	1.1×10^{-4}	2.6×10^3	1.4×10^{-3}	2.5×10^3
2048	4.8×10^{-5}	2.6×10^3	4.4×10^{-4}	2.5×10^3
4096	1.4×10^{-5}	2.5×10^3	5.4×10^{-4}	2.5×10^3
8192	Reference	2.5×10^3	Reference	2.4×10^3

Table VII. Convergence of the population dynamics obtained for the polaron-transformed MSB models with varying numbers of TLSs, M , as a function of the number of frequencies used in the discretized bath, N . Convergence is measured through the average relative deviation of the population dynamics from the reference calculations indicated in the Table. We also present the average number of Hamiltonian evaluations per node required to obtain this dynamics out to a time $t\Delta = 6$.

of the deviation to less than 10^{-4} is not obtained until there are $N = 2048$ distinct frequencies in the bath. For $M = 2$, the deviations between the results obtained with $N = 4096$ and $N = 8192$ distinct frequencies are larger than 10^{-4} . These correspond to calculations with 8,192 and 16,384 bath modes, respectively, which demonstrates that there are models for which very large number of bath modes are required to obtain accurate results. The significant increase in the number of bath modes required when moving from $M = 1$ to $M = 2$ can be understood in terms of the increased complexity in the bath correlation functions present. In order to accurately describe the effect of the bath on the system dynamics it is necessary to have sufficiently many bath modes so that the resultant Fourier series approximation of each distinct bath correlation function is accurate. As we increase the number of bath correlation functions and the allow for different functional forms, which occurs as we increase the number of TLSs M , we need more bath modes to obtain the same accuracy.

These results also demonstrate that the calculations presented in the main text are not converged to the continuum bath limit. However, for the fixed $N = 512$ model they have been converged with respect to all other parameters. For the $M = 4$ and $M = 6$ cases we would expect similar results, that is the dynamics is not converged to the continuum bath limit and large numbers of bath modes would be required to do so.

B. Polaron-Transformed Multi-Spin-Boson Model

As a final application of the PSI approach we will consider the polaron-transformed form of the multi-spin-boson model Hamiltonian that was considered in Sec. III.C of Paper II. Using a transformation

$$\hat{T} = \exp \left[- \sum_{i=1}^M \hat{\sigma}_{i,z} \sum_k \frac{g_{ik}}{\omega_k} \left(\hat{a}_k^\dagger - \hat{a}_k \right) \right] \quad (74)$$

that displaces the bath modes depending on the states of each of the TLSs, and applying this transform to the Hamiltonian in Eq. 39 of Paper II gives

$$\begin{aligned} \hat{H}_{pol} &= \hat{T}^\dagger \hat{H} \hat{T} \\ &= \sum_{i=1}^M \varepsilon_i \hat{\sigma}_{i,z} - \sum_{i,j=1}^M J_{ij} \hat{\sigma}_{i,z} \hat{\sigma}_{j,z} + \sum_k \omega_k \hat{a}_k^\dagger \hat{a}_k + \sum_{i=1}^M \Delta_i \left[\hat{\sigma}_{i,+} \exp \left[-2 \sum_k \frac{g_{ik}}{\omega_k} (\hat{a}_k^\dagger - \hat{a}_k) \right] + \text{h.c.} \right], \end{aligned} \quad (75)$$

where the TLS-TLS coupling constant is given by

$$J_{ij} = \frac{1}{\hbar} \sum_k \frac{g_{ik} g_{jk}}{\omega_k} = \frac{1}{\pi \hbar} \int_0^\infty \frac{J_{ij}(\omega)}{\omega} d\omega. \quad (76)$$

The polaron transform introduces a direct coupling between the TLSs in this model, as well as a set of terms that directly couple all bath modes to each other in a multiplicative fashion and to each of the TLSs.

We now present the population dynamics for polaron-transformed MSB models with one or two TLSs that have been obtained using the PSI with ML-MCTDH wavefunctions that make use of varying numbers of SPFs. These results are shown in Table VIII. We have used the same tree topologies as were used in Sec. III.C of Paper II for the standard representation of the MSB Hamiltonian, and all calculations presented in this section were obtained with a time step of $dt\Delta = 0.04$. When evaluating the deviations in the population dynamics, we have used the same references as were used in the main text. Namely, we have used the results obtained using the standard Hamiltonian and $N_{spf} = 48$ and 80 when $M = 1$ and 2, respectively. These results are entirely analogous to those presented in Table V of Paper II, however, now using the polaron-transformed representation for the Hamiltonian.

M	1		2	
N_{spf}	$\langle \Delta P \rangle$	$\langle N_H \rangle$	$\langle \Delta P \rangle$	$\langle N_H \rangle$
4	1.6×10^{-2}	2.3×10^3	2.5×10^{-2}	2.2×10^3
8	5.7×10^{-4}	2.6×10^3	1.1×10^{-1}	2.5×10^3
12	4.5×10^{-5}	2.9×10^3	6.4×10^{-3}	2.7×10^3
16	1.5×10^{-5}	3.1×10^3	3.0×10^{-3}	2.8×10^3
24	2.1×10^{-6}	3.1×10^3	2.0×10^{-3}	3.0×10^3
32	7.3×10^{-7}	3.4×10^3	7.7×10^{-4}	3.2×10^3
48	4.7×10^{-7}	4.0×10^3	4.3×10^{-4}	3.8×10^3
64			5.5×10^{-5}	4.0×10^3

Table VIII. Convergence of the population dynamics obtained for the polaron-transformed MSB models with varying numbers of TLSs, M , as a function of the number of SPFs, N_{spf} . Convergence is measured through the average relative deviation of the population dynamics from the reference calculations indicated in Table V of Paper II that were obtained using the standard representation for this Hamiltonian. We also present the average number of Hamiltonian evaluations per node required to obtain this dynamics out to a time $t\Delta = 6$.

For both $M = 1$ and $M = 2$ the deviations from the reference calculations, which were obtained using the standard representation of the MSB model, decrease with increasing numbers of SPFs. As such, the dynamics we obtain using the PSI converge towards the same result regardless of the representation used, as expected. This supports the notion that we are converging towards the correct dynamics. For $M = 1$ we find deviations of less than 10^{-4} for all $N_{spf} \geq 12$, while for $M = 2$ we find that $N_{spf} = 64$ is required. For the $M = 1$ case, the deviations obtained for a given N_{spf} are comparable to those obtained using the standard representation (Table V of Paper II), however, typically more Hamiltonian evaluations are required. For $M = 2$, we find slightly larger deviations at a given N_{spf} when using the polaron-transformed model, as well as larger numbers of Hamiltonian applications being required. For this problem, the polaron-transform increases the cost of the calculations.

REFERENCES

- ¹M. Beck, A. Jäckle, G. Worth, and H.-D. Meyer, Phys. Rep. **324**, 1 (2000).
- ²M. H. Beck and H.-D. Meyer, Z. Phys. D **42**, 113 (1997).
- ³U. Manthe, Chem. Phys. **329**, 168 (2006).
- ⁴C. Lubich, Appl. Math. Res. Express **2015**, 311 (2015).
- ⁵B. Kloss, I. Burghardt, and C. Lubich, J. Chem. Phys. **146**, 174107 (2017).
- ⁶M. Bonfanti and I. Burghardt, Chem. Phys. **515**, 252 (2018).

- ⁷E. Kieri, C. Lubich, and H. Walach, *SIAM J. Numer. Anal.* **54**, 1020 (2016).
- ⁸G. Ceruti, C. Lubich, and H. Walach, *SIAM J. Numer. Anal.* **59**, 289 (2021).
- ⁹G. Ceruti and C. Lubich, *BIT Numer. Math.* , 1 (2021).
- ¹⁰T. Weike and U. Manthe, *J. Chem. Phys.* **154**, 194108 (2021).
- ¹¹H. Wang and H.-D. Meyer, *J. Chem. Phys.* **149**, 044119 (2018).
- ¹²H. Wang and M. Thoss, *J. Chem. Phys.* **119**, 1289 (2003).
- ¹³U. Manthe, *J. Chem. Phys.* **128**, 164116 (2008).
- ¹⁴R. B. Sidje, *ACM Trans. Math. Softw.* **24**, 130 (1998).
- ¹⁵H. Wang and H.-D. Meyer, *J. Phys. Chem. A* **125**, 3077 (2021).
- ¹⁶H.-D. Meyer and H. Wang, *J. Chem. Phys.* **148**, 124105 (2018).